

32 absorption, solubility, etc., thus knowledge of the chemical composition and mixing state of the
33 aerosol particles is important for modeling of aerosol impact (Boucher et al., 2013). The aerosol
34 properties may vary in a wide range, so in practice usually several main types of aerosols are
35 separated on a base of their origin: e.g. urban, dust, marine, biomass burning (Dubovik et al., 2002).
36 Successful remote characterization of column integrated aerosol composition from the
37 observations of Sun – sky photometers and space-borne multiangle polarimeters was demonstrated
38 in numerous publications (Dubovik et al., 2002; Giles et al., 2012; Hamill et al., 2016; Schuster et
39 al., 2016; Li et al., 2019; Zhang et al., 2020). The aerosol impacts, however, depends also on
40 vertical variations/distributions of particle concentration and composition, which cannot be
41 derived from these instruments.

42 One of the recognized remote sensing techniques for vertical profiling of aerosol properties
43 is a lidar. Multiwavelength Mie-Raman and HSRL (High Spectral Resolution Lidar) lidar systems
44 provide unique opportunity to derive height-resolved particle intensive properties, such as lidar
45 ratios, Angstrom exponents and depolarization ratios at multiple wavelengths. Based on this
46 information, particle type can be determined (Burton et al., 2012, 2013; Groß et al., 2013; Mamouri
47 et al., 2017; Papagiannopoulos et al., 2018; Nicolae et al., 2018; Hara et al., 2018; Voudouri et al.,
48 2019; Wang et al., 2021; Mylonaki et al., 2021 and references therein). However, there is a
49 fundamental difference between particle classification based on the Sun – sky photometer and on
50 lidar observations. From both direct Sun and azimuth scanning measurements of the photometer
51 more than 100 observations are available. From this information the spectrally dependent
52 refractive index and absorption Angstrom exponent can be determined, which is important for
53 aerosol classification (Schuster et al., 2016; Li et al., 2019). The commonly used multiwavelength
54 lidars are based on a tripled Nd:YAG laser and are capable of providing three backscattering (355
55 nm, 532 nm, 1064 nm), two extinction (355 nm, 532 nm) coefficients and up to three particle
56 depolarization ratios (so called $3\beta+2\alpha+3\delta$ set). Thus the number of available lidar observations is
57 eight or less, which limits the performance of the aerosol typing algorithms. Nevertheless, the
58 results obtained by different research groups demonstrate that lidar-based particle identification is
59 possible. In publications of Burton et al. (2012, 2013) classification was performed from four
60 intensive parameters measured by the HSRL system: the lidar ratio at 532 nm (S_{532}), the
61 backscattering Angstrom exponent for 532/1064 nm wavelengths ($BAE_{532/1064}$), and particle
62 depolarization ratios at 532 nm and 1064 nm (δ_{532} , and δ_{1064}). With these input parameters eight

63 aerosol types: smoke, fresh smoke, urban, polluted maritime, maritime, dusty mix, pure dust and
64 ice were discriminated.

65 Important information on aerosol vertical distribution comes from the
66 EARLINET/ACTRIS lidar-network, aiming at unifying multiwavelength Mie-Raman lidar
67 systems over Europe (Pappalardo et al., 2014). For the automation of aerosol classification, several
68 approaches were developed in the frame of EARLINET. These approaches include the
69 Mahalanobis distance-based typing algorithm (Papagiannopoulos et al., 2018), a neural network
70 aerosol classification algorithm (NATALI) (Nicolae et al., 2018), and algorithm based on source
71 classification analysis (SCAN) (Mylonaki et al., 2021). All these algorithms have demonstrated
72 their ability for aerosol classification. In particular, the NATALI is able to identify up to 14 aerosol
73 mixtures from $3\beta+2\alpha+1\delta$ observations.

74 Nevertheless, the above-mentioned algorithms have to deal with a fundamental limitation:
75 the particle intensive properties, even for pure aerosols (generated by a single source) exhibit
76 strong variations. For example, the lidar ratio S_{355} of smoke in publication of Nicolae et al. (2018)
77 varies in 38 sr – 70 sr range, and in our own measurements we observed for aged smoke S_{355} as
78 low as 25 sr (Hu et al., 2021). Strong variation of smoke lidar ratios in EARLINET/ACTRIS
79 observations is discussed also in the recent publication of Adam et al. (2021). Such uncertainty in
80 parameters of the aerosol model complicates the aerosol classification. Thus, it is desirable to
81 combine the Mie-Raman observations with another range resolved technique, providing additional
82 independent information about aerosol composition. Such information can be obtained from laser
83 induced fluorescence emission.

84 Application of fluorescence lidar technique was intensively considered during the last
85 decade to study aerosol particles. Lidar measurements of the full fluorescence spectrum with
86 multianode photomultipliers (Sugimoto et al., 2012; Reichardt et al., 2014, 2017; Saito et al., 2022)
87 provides an obvious advantage in particle identification. However, even a more simple
88 fluorescence lidar with a single wideband fluorescence channel, opens new opportunities for
89 aerosol characterization (Veselovskii et al., 2021; 2022; Zhang et al., 2021). Such fluorescence
90 configuration could be implemented in existing Mie-Raman lidars, and the fluorescence
91 backscattering coefficient β_F is calculated from the ratio of fluorescence and nitrogen Raman
92 signals. To characterize the aerosol fluorescence properties, the fluorescence capacity G_F is
93 introduced as the ratio of β_F to aerosol backscattering coefficient at one of laser wavelengths

94 (Veselovskii et al., 2020b). In this study, the backscattering at 532 nm was used. The fluorescence
95 capacity is an intensive particle parameter, which changes strongly with aerosol type, being the
96 highest for smoke and the lowest for dust. Thus, the combination of Mie – Raman and fluorescence
97 backscatter provides a basis to improve particle classification. A Mie – Raman lidar provides
98 several particle intensive parameters, however, the profiles of particle parameters associated with
99 the extinction coefficient, such as lidar ratio or extinction Angstrom exponent, may contain strong
100 noises, because the extinction coefficients are derived from the slope of Raman lidar signals, thus
101 averaging over significant spatio-temporal intervals is demanded. Meanwhile, the particle
102 depolarization and the fluorescence *capacity* can be calculated with high spatio-temporal
103 resolution.

104 Recently, we have demonstrated that the $\delta - G_F$ diagram allows to separate several aerosol
105 types, such as dust, pollen, urban (continental) and smoke (Veselovskii et al., 2021a). In the present
106 study, we use this technique to classify aerosol particle types in the troposphere at high spatio-
107 temporal resolution. We present results of aerosol classification on the basis of fluorescence and
108 Mie-Raman lidar measurements performed at the ATOLL (ATmospheric Observation at liLLe) at
109 Laboratoire d’Optique Atmosphérique, University of Lille, during 2020 – 2021 period, which
110 includes strong smoke, dust and pollen episodes. Paper starts with a description of the experimental
111 setup and data processing scheme in Sect.2. In Sect.3 we present the algorithm for aerosol
112 classification on a base of depolarization and fluorescence measurements. Results of the
113 application of the developed approach to different atmospheric situations, including smoke, dust
114 and pollen episodes are given in Sect.4.

115

116 **2. Experimental setup and data analysis**

117 **2.1. Lidar system**

118 The multiwavelength Mie-Raman lidar LILAS (Lille Lidar AtmosphereS) is based on a
119 tripled Nd:YAG laser with a 20 Hz repetition rate and pulse energy of 70 mJ at 355 nm.
120 Backscattered light is collected by a 40 cm aperture Newtonian telescope and the lidar signals are
121 digitized with Licel transient recorders with 7.5 m range resolution, allowing simultaneous
122 detection in the analog and photon counting mode. The system is designed for the detection of
123 elastic and Raman backscattering, allowing the so called $3\beta+2\alpha+3\delta$ data configuration, including
124 three particle backscattering (β_{355} , β_{532} , β_{1064}), two extinction (α_{355} , α_{532}) coefficients along with

125 three particle depolarization ratios (δ_{355} , δ_{532} , δ_{1064}). The particle depolarization ratio, determined
126 as a ratio of cross- and co-polarized components of the particle backscattering coefficient, was
127 calculated and calibrated in the same way as described in Freudenthaler et al. (2009). Many
128 calibration and operation procedures have been automated for the LILAS system to improve the
129 overall performance of the lidar in terms of observation frequency and data quality. The aerosol
130 extinction and backscattering coefficients at 355 and 532 nm were calculated from Mie-Raman
131 observations (Ansmann et al., 1992), while β_{1064} was derived by the Klett method (Klett, 1985).
132 The full geometrical overlap was achieved at approximately 750 m range. For calculation of α and
133 β at 532 nm we use the rotational Raman scattering instead of the vibrational one (Veselovskii et
134 al., 2015), which allows to increase the power of Raman backscatter and to decrease separation
135 between the wavelengths of elastic and Raman components. Additional information about
136 atmospheric parameters was available from radiosonde measurements performed at Herstmonceux
137 (UK) and Beauvechain (Belgium) stations, located 160 km and 80 km away from the observation
138 site respectively.

139 The LILAS system can also profile the laser induced fluorescence of aerosol particles. A
140 part of the fluorescence spectrum is selected by a wideband interference filter of 44 nm width
141 centered at 466 nm. The strong sunlight background at daytime restricts the fluorescence
142 observations to nighttime hours. The fluorescence backscattering coefficient β_F , is calculated from
143 the ratio of fluorescence and nitrogen Raman backscattering signal, as described in Veselovskii et
144 al. (2020b). This approach allows us to evaluate the absolute values of β_F , if the relative sensitivity
145 of the channels is calibrated and the nitrogen Raman scattering differential cross section is known.
146 All β_F profiles presented in this work were smoothed with the Savitzky – Golay method, using
147 second order polynomials with 21 points in the window. For the calculation of the fluorescence
148 capacity G_F , in principle, backscattering coefficients at any laser wavelength can be used. In our
149 study we always used β_{532} , because it is calculated with the use of rotational Raman component

150 and is considered to be the most reliable, thus the fluorescence capacity is calculated as $G_F = \frac{\beta_F}{\beta_{532}}$.

151 ***2.2. Calculation of the particle backscattering coefficient from Mie-Raman measurements***

152 Mie – Raman lidar measurements allow independent evaluation of aerosol extinction and
153 backscattering coefficients. Commonly used approach for β calculation was formulated in the
154 paper of Ansmann et al. (1992). This approach includes the choice of a reference height, where the

155 scattering is purely molecular. However, such height range is not always available, for example,
 156 in the presence of the low level clouds. Moreover, when long-term spatio-temporal variations of
 157 backscattering coefficients are analyzed, the uncertainty in the choice of the reference height leads
 158 to oscillations in β profiles. To resolve this issue, we modified the Raman method as described
 159 below.

160 In an elastic channel, the backscattered radiative power P_L , at wavelength λ_0 and distance
 161 z is described by the lidar equation:

$$162 \quad P_L = O(z) \frac{1}{z^2} C_L (\beta_L^a + \beta_L^m) \exp \left\{ -2 \int_0^z (\alpha_L^a + \alpha_L^m) dz' \right\} = O(z) \frac{1}{z^2} C_L (\beta_L^a + \beta_L^m) T_L^2, \quad (1)$$

163 while in a Raman channel, it can be written as:

$$164 \quad P_R = O(z) \frac{1}{z^2} C_R \beta_R \exp \left\{ - \int_0^z (\alpha_L^a + \alpha_R^a + \alpha_L^m + \alpha_R^m) dz' \right\} = O(z) \frac{1}{z^2} C_R \beta_R T_L T_R. \quad (2)$$

165 Here $O(z)$ is the geometrical overlap factor, which is assumed to be the same for elastic and Raman
 166 channels. C_L and C_R are the range independent constants, including efficiency of the detection
 167 channel. T_L and T_R are one-way transmissions, describing light losses on the way from the lidar to
 168 distance z at laser λ_L and Raman λ_R wavelengths. Backscattering and extinction coefficients contain
 169 aerosol and molecular contributions: $\beta_L^a + \beta_L^m$ and $\alpha_L^a + \alpha_L^m$, where the superscripts “a” and “m”
 170 indicate aerosol and molecular scattering, respectively. Raman backscattering coefficient is:

$$171 \quad \beta_R = N \sigma_R, \quad (3)$$

172 where N is the number of Raman scatters (per unit of volume) and σ_R is the Raman differential
 173 scattering cross section in the backward direction.

174 Dividing equation (1) on (2) we get:

$$175 \quad \frac{P_L}{P_R} = \frac{C_L}{C_R} \frac{(\beta_L^a + \beta_L^m) T_L}{\beta_R T_R} \quad (4)$$

176 Backscattering coefficient is calculated from (3) and (4) as:

$$177 \quad \beta_L^a = \frac{P_L}{P_R} \frac{C_R}{C_L} \sigma_R N \frac{T_R}{T_L} - \beta_L^m = \frac{P_L}{P_R} KN \frac{T_R}{T_L} - \beta_L^m \quad (5)$$

178 The differential transmission $\frac{T_L}{T_R}$ can be calculated the same way, as it is done for the water vapor
 179 measurements (Whiteman, 2003). For rotational Raman signal, which we use in our 532 nm
 180 channel (Veselovskii et al., 2015), $\lambda_L \approx \lambda_R$, so $\frac{T_L}{T_R} = 1$.

181 The calibration constant $K = \frac{C_R}{C_L} \sigma_R$ can be found by comparing β_L^a in Eq.5 with the
 182 backscattering coefficient $\tilde{\beta}_L^a$ computed with the traditional Raman method, using the reference
 183 height (Ansmann et al., 1992).

$$184 \quad K = (\tilde{\beta}_L^a + \beta_L^m) \frac{P_R}{P_L} \frac{1}{N} \frac{T_L}{T_R} \quad (6)$$

185 For simplicity, hereinafter we will use notation β_L instead β_L^a . Thus, if during the measurement
 186 session we have a temporal interval, where the reference height is available, we can determine the
 187 calibration constant K and use it for β_L calculations from eq.5, assuming that relative sensitivity of
 188 channels during the session is not changed. Even if cloud layers occur during the whole session,
 189 we can use K from the previous cloud-free profiles (assuming, again, that the relative sensitivity
 190 of channels is the same). We will call this approach for β calculation as “modified Raman method”,
 191 to distinguish it from traditional one (Ansmann et al., 1992).

192 To estimate variations of the relative sensitivity of the channels, we analyzed long-term
 193 cloudless measurements when the reference height was available for every individual profile. The
 194 results demonstrate that variations of calibration constant during the session (about 8 hours) were
 195 below 3%. Fig.1 and 2 present the application of this modified Raman method to the measurements
 196 on 2 March 2021. The dust layer extended from 2 km to 8 km height and inside this layer the ice
 197 and liquid clouds were formed during the 00:00 – 05:00 UTC interval, thus β_{532} could not be
 198 calculated with traditional Raman technique. The temporal interval 19:00 – 20:00 was used to find
 199 calibration constant K . Fig.1 shows vertical profiles of backscattering coefficient $\tilde{\beta}_{532}$ calculated
 200 with traditional Raman method (with reference height), and β_{532} calculated with modified method
 201 (with the calibration constant). Profiles of $\tilde{\beta}_{532}$ and β_{532} coincide for the whole height range. The
 202 calibration constant K , shown on the same plot, does not demonstrate height dependence, though

203 oscillations around the mean value increase with height. For computations, we choose the value of
204 K at low altitudes averaged inside some height interval.

205 Fig.2 provides spatio-temporal variations of β_{532} , particle depolarization δ_{532} and the
206 fluorescence capacity G_F . Depolarization measurements reveal the presence of dust ($\delta_{532}\approx 30\%$)
207 and the ice cloud above 4 km ($\delta_{532}>40\%$). The liquid cloud below 4 km after midnight can be
208 identified by a low depolarization ratio $\delta_{532}<3\%$. The fluorescence capacity of dust is low, about
209 0.2×10^{-4} . However, below 2 km, G_F is significantly higher, up to 1.2×10^{-4} . In combination with a
210 high depolarization ratio (up to 20%), it can indicate the presence of pollen at low altitudes. On
211 the fluorescence capacity panel, we can see that after 01:00 UTC the dust and pollen layers are
212 mixed below 2 km, resulting in a value of G_F about 0.5×10^{-4} . The fluorescence capacity inside ice
213 and liquid clouds is below 0.01×10^{-4} . Fig.2 clearly demonstrates the advantage of simultaneous
214 depolarization and fluorescence measurements for the study of cloud formation in the presence of
215 aerosol. All spatio-temporal distributions of β_{532} presented in this paper were calculated from Eq.5
216 with a modified Raman method.

217

218 **3. Aerosol classification based on fluorescence measurements**

219 **3.1. Approach for aerosol classification.**

220 As was discussed in our recent publication (Veselovskii et al., 2021), the δ - G_F diagram
221 allows to separate several aerosol types, including smoke, dust, pollen, urban, ice and liquid water
222 particles. Smoke and urban aerosols both have a small depolarization ratio, but the fluorescence
223 capacity of smoke is almost one order higher, so these particles can be separated. Dust and pollen
224 both have high depolarization ratio (up to 30%), but G_F of dust is significantly lower, which again
225 provides basis for discrimination. The depolarization ratio of some aerosol types is characterized
226 by strong spectral dependence. For example, the depolarization ratio of aged smoke decreases with
227 wavelength. It is below 5% at 1064 nm but at 355 nm in upper troposphere it may exceed 20%
228 (Burton et al., 2015; Haarig et al., 2018; Hu et al., 2019; Veselovskii et al., 2022), which
229 complicates smoke and dust separation. For pollen, on the contrary, the depolarization ratio at
230 1064 nm can be the highest (Veselovskii et al., 2021). Thus, choice of δ_{1064} for δ - G_F diagram could
231 be advantageous. However, as mentioned, the backscattering coefficient at 1064 nm is calculated
232 with Klett method (Klett, 1985), which, besides assumption about lidar ratio, needs reference

233 height and cannot be used in cloudy situations. This is why in our study we used the δ_{532} - G_F
234 diagram.

235 In our present work, we consider a simple classification scheme since we use only two
236 intensive parameters G_F and δ_{532} . Our goal is to demonstrate that in the δ_{532} - G_F diagram, our lidar
237 observations form clusters and characteristic patterns which can be attributed to different aerosol
238 types or their mixtures. We consider four aerosol types: dust, smoke, pollen and urban, and two
239 cloud types: liquid and ice clouds. Dust and pollen are large particles of complicated shape,
240 characterized by high depolarization ratio, while smoke and urban pollution are small particles
241 with low depolarization. In our classification “urban aerosol” includes continental aerosol, sulfates
242 and soot. At this stage, we do not yet consider absorption to discriminate particles.

243 The choice of the range of particle properties variation for each aerosol type is an important
244 aspect of the approach. Typical ranges of G_F and δ_{532} variations used in our classification scheme
245 are given in Table 1 and are shown in Fig.3. These ranges are based on results obtained in LOA
246 (Laboratoire d’Optique Atmosphérique) and on results presented in aerosol classification studies
247 (Burton et al., 2012, 2013; Nicolae et al., 2018; Papagiannopoulos et al., 2018, Mylonaki et al.,
248 2021).

249 **Dust.** The depolarization ratio, δ_{532} , of Saharan dust near the source regions is up to 35%
250 (Veselovskii et al., 2020a). However, after transportation and mixing with local aerosol δ_{532} can
251 be as low as 20% (Rittmeister et al., 2017). In many studies, the dust events having with smaller
252 depolarization ratio are classified as “polluted dust” (e.g. Burton et al., 2012, 2013). At the moment,
253 we do not introduce the discrimination between the two subtypes and mark as “dust” the particles
254 with $20\% < \delta_{532} < 35\%$, and $0.1 \times 10^{-4} < G_F < 0.5 \times 10^{-4}$.

255 **Smoke.** In 2021-2022, we regularly observed, over ATOLL platform, smoke layers
256 originated from Californian and Canadian forest fires (Hu et al., 2022). The particle depolarization
257 and fluorescence capacity of this transported smoke varied from episode to episode and, for
258 classification, we selected the ranges $2\% < \delta_{532} < 10\%$, $2 \times 10^{-4} < G_F < 6 \times 10^{-4}$. At this stage, we do not
259 discriminate “fresh” and “aged” smoke, and the range of δ_{532} variation is similar to the one used
260 in classification of Burton et al. (2012).

261 **Pollen.** The pollen over north of France is usually mixed with other aerosol and the
262 particles which we mark as “pollen” are actually the mixtures. Depolarization ratio of clean pollen
263 varies strongly for different taxa. For birch pollen, Cao et al. (2010) reported $\delta_{532}=33\%$, and in the

264 measurements over Finland during birch pollination (Bohlmann et al., 2019), observed values of
 265 δ_{532} up to 26%. The observations over Lille during pollen season (Veselovskii et al., 2021a) rarely
 266 revealed values δ_{532} exceeding 20%. Based on that observations, we type as “pollen” the particles
 267 mixtures with $15\% < \delta_{532} < 30\%$, and $0.8 \times 10^{-4} < G_F < 3.0 \times 10^{-4}$.

268 **Urban.** This type of aerosol includes a variety of particle types (e.g. sulfates, soot) and its
 269 properties may depend on the relative humidity. Based on our measurements inside the boundary
 270 layer, for classification we choose the ranges $1\% < \delta_{532} < 10\%$, and $0.1 \times 10^{-4} < G_F < 1.0 \times 10^{-4}$. Similar
 271 range for δ_{532} is used in classification of Burton et al. (2013). Urban and smoke particles both have
 272 a low depolarization, but the smoke fluorescence capacity can be up to one order higher, so these
 273 particles can be reliably discriminated.

274 **Ice and water clouds.** Both cloud types have low fluorescence capacity $G_F < 0.01 \times 10^{-4}$.
 275 However, the ice clouds are usually observed at the heights, where fluorescence signal is low and
 276 can not be used for classification. Thus above ~ 8 km, the ice cloud are identified by high
 277 depolarization ratio $\delta_{532} > 40\%$. Depolarization ratio of the liquid water clouds is usually affected
 278 by the effects of the multiple scattering, so for their identification we use $\delta_{532} < 5\%$.

279 The analysis of aerosol mixtures is an important subject and, the possibility to separate the
 280 mixture components based on lidar measurements was discussed in publications of Sugimoto and
 281 Lee (2006), Gross et al. (2011), Gasteiger et al. (2011), Tesche et al. (2009), Burton et al. (2014).
 282 The information about mixture composition can be also revealed in δ_{532} - G_F diagram. For example,
 283 pollen can be mixed with urban particles. At different heights the pollen contributes differently to
 284 β_{532} , so at δ_{532} - G_F diagram, the data points will form the pattern, which extends from location,
 285 attributed to “pure” urban aerosol to location, attributed to “pure” pollen. To estimate, how such
 286 pattern looks like, a simplified modeling for fixed particle parameters was performed.
 287 Corresponding results are shown in Fig.3 by symbols (circles). The particle depolarization ratio δ
 288 of the mixture, containing urban aerosol (u) and pollen (p), with depolarization ratios δ^u and δ^p ,
 289 can be calculated as:

$$290 \quad \delta = \frac{\left(\frac{\delta^p}{1 + \delta^p}\right)\beta^p + \left(\frac{\delta^u}{1 + \delta^u}\right)\beta^u}{\frac{\beta^p}{1 + \delta^p} + \frac{\beta^u}{1 + \delta^u}} \quad (7)$$

291 The fluorescence capacity of the mixture is given by:

292
$$G_F = \frac{\beta^u G_F^u + \beta^p G_F^p}{\beta} \quad (8)$$

293 Here total backscattering $\beta = \beta^u + \beta^p$.

294 The computations in Fig.3 were performed for values of pollen contribution $\frac{\beta_{532}^p}{\beta_{532}}$ in 0 - 1.0
 295 range with step 0.1. We assume that the depolarization ratios of pollen and urban aerosol are δ_{532}^p
 296 =30% and $\delta_{532}^u=3\%$, while the fluorescence capacities are $G_F^u=0.2\times 10^{-4}$ and $G_F^p=2.5\times 10^{-4}$. We
 297 remind that the fluorescence capacities are calculated at 532 nm wavelength. In the $\delta_{532}-G_F$
 298 diagram the computed points provide a characteristic curve, which in the next section will be
 299 compared with experimental results. The same computations were performed for a smoke (s) and
 300 dust (d) mixture, assuming $\delta_{532}^d=30\%$, $\delta_{532}^s=3\%$, $G_F^d=0.2\times 10^{-4}$ and $G_F^s=4.0\times 10^{-4}$. Corresponding
 301 results are shown in Fig.3 with stars. In a similar way, the characteristic curves for other mixtures
 302 can be also represented.

303 We are also able to identify liquid water and ice layers. Liquid water cloud layers have low
 304 fluorescence capacity ($G_F<0.01\times 10^{-4}$) and $\delta_{532}<3\%$. Ice particles also have low G_F , but at heights
 305 where ice clouds are usually observed, the signal of fluorescence backscattering is noisy. Thus at
 306 high altitudes ice particles are discriminated by a high depolarization ratio $\delta_{532}>40\%$.

307

308 **3.2. Classification of spatio-temporal observations**

309 The input parameters in our classification scheme are the spatio-temporal distributions of β_{532} ,
 310 δ_{532} and G_F , which are presented as matrices $\beta_{532}^{i,j}$, $\delta_{532}^{i,j}$, $G_F^{i,j}$, where $i=1\dots N_T$; $j=1\dots N_H$. Values
 311 N_T and N_H are the numbers of temporal and height intervals in the analyzed dataset. In a single
 312 measurement we accumulate 2×10^3 laser pulses, so temporal resolution of the measurements is
 313 about 100 s, while the height resolution is 7.5 m.

314 The particle intensive properties cannot be evaluated reliably when the backscattering
 315 coefficient is low. Thus, we set a threshold value for β_{532} (normally $0.2 \text{ Mm}^{-1}\text{sr}^{-1}$); namely, when
 316 $\beta_{532}^{i,j} < 0.2 \text{ Mm}^{-1}\text{sr}^{-1}$ the elements of the matrices $\delta_{532}^{i,j}$ and $G_F^{i,j}$, are classified as “low signal” and
 317 ignored. For the remaining elements, we determine the aerosol type, using our approach. A primary
 318 typing is being made for each point (i,j) separately, in accordance with parameter ranges given in

319 the Table 1. The elements, which are out of all these ranges, are marked as “undefined”. We
 320 consider 6 types of the particles, respectively dust, smoke, pollen, urban, ice crystals and water
 321 droplets. Moreover, there can be two additional results of primary typing: “undefined” and “low
 322 signal”. Thus, there are altogether 8 possible results of primary typing. For every aerosol type, a
 323 $N_T \times N_H$ dimension matrix is constructed. If at this first stage of classification some single pixel
 324 point (i, j) is classified as, e.g., dust, the corresponding value in the 'dust' matrix is set to 1,
 325 otherwise it is set to 0.

326 The single pixel particle parameters contain statistical noise, which influences the results of
 327 the primary typing, thus producing high frequency oscillations of non-physical character. From a
 328 physical point of view, the aerosol single-type areas should form smooth regions, so a special
 329 smoothing procedure (stage 2 of our algorithm) was developed to remove the oscillations. The
 330 smoothing procedure is based on a convolution with Gaussian kernel

$$331 \quad Z = \exp\left(-\left(\frac{t^2}{s_T^2} + \frac{h^2}{s_H^2}\right)\right) \quad (9)$$

332 where t and h are temporal and height coordinates. The resolution of typing is being controlled by
 333 the parameters s_T and s_H , which are set as the number of temporal and height bins.

334 On the second stage of classification each of these matrices is separately convoluted with
 335 the Gauss kernel Z . After the convolution, the values for each pixel (i,j) are being compared. If,
 336 e.g., the 'dust' matrix contains maximal value at the pixel (i,j), in respect to all other matrices, then
 337 the pixel (i,j) is finally classified as dust. The choice of smoothing parameters depends on aerosol
 338 loading and aerosol type. For the measurements inside the boundary layer in many cases the single
 339 pixel typing ($s_T=1$, $s_H=1$) is possible, while for analysis of the weak elevated layers the smoothing
 340 should be applied. All results presented in this study were obtained for $s_T=3$ and $s_H=5$, thus the
 341 temporal and range resolutions of our typing procedure are estimated to be about 8 minutes and
 342 60 m respectively.

343

344 **4. Application of classification approach to LILAS data**

345 The classification approach, described in the previous section, was applied to the data of
 346 the Mie-Raman- Fluorescence lidar at the ATOLL platform, located on the campus of Lille
 347 University, during 2020 – 2021 period. Here we present results of aerosol classification for several

348 relevant atmospheric situations, to demonstrate that different aerosol types are well separated
349 based on δ_{532} - G_F diagram.

350 ***12 September 2020: Wildfire smoke***

351 Fig.4 presents the spatio-temporal variations of aerosol and fluorescence backscattering
352 coefficients (β_{532} and β_F) together with the particle depolarization ratio δ_{532} and the fluorescence
353 capacity G_F during smoke episode on the night 12-13 September 2020. The smoke layer extends
354 from approximately 2 km to 5 km height, and it is characterized by high fluorescence capacity
355 $G_F > 3.0 \times 10^{-4}$ and low depolarization ratio $\delta_{532} < 7\%$. The cirrus clouds occurred above 11 km height
356 during the whole night. The smoke layer was transported from North America; detailed analysis
357 of the layer origin and transportation is given in the recent publication of Hu et al. (2022). The
358 results of aerosol typing for this episode are shown in Fig.5. On the δ_{532} - G_F diagram these data
359 form two clusters. First cluster includes points in the range $2.0 \times 10^{-4} < G_F < 6.0 \times 10^{-4}$ and
360 $2\% < \delta_{532} < 7\%$, such high fluorescence and low depolarization should be attributed to smoke
361 particles. The second cluster consists of points localized inside $0.1 \times 10^{-4} < G_F < 0.8 \times 10^{-4}$ and
362 $1\% < \delta_{532} < 3\%$ intervals which corresponds to urban particles in Table 1. After cluster localization,
363 the observations can be plotted as aerosol types, using the parameters in Table 1 and the approach,
364 described in section 3.2. The aerosol types in Fig.5b are spatially separated and contain no high
365 frequency oscillations. Urban particles are localized at low heights, below 1 km. We would like to
366 remind that, at the condition of high relative humidity (RH), the fluorescence capacity can decrease
367 due to the particle's hygroscopic growth (Veselovskii et al., 2020). In accordance with radiosonde
368 data the relative humidity below 1 km was quite high (about 70% at 500 m) and decreased with
369 height, which can explain the wide range of G_F variation observed for urban particles in Fig.5a.

370 The particle intensive properties, such as the lidar ratios at 355 nm and 532 nm wavelengths
371 (S_{355} , S_{532}), the particle depolarization ratios (δ_{355} , δ_{532} , δ_{1064}), the extinction ($A_{355/532}^\alpha$) and the
372 backscattering ($A_{355/532}^\beta$, $A_{532/1064}^\beta$) Angstrom exponents for the episodes analyzed in this study, are
373 summarized in Table 2. For this measurement session, in the smoke layer the lidar ratio at 532 nm
374 significantly exceeds corresponding value at 355 nm ($S_{532} = 80 \pm 12$ sr and $S_{355} = 50 \pm 7$ sr). The
375 particle depolarization ratio decreases with wavelength from 4.5% at 355 nm to 2% at 1064 nm.
376 Such spectral dependence of the lidar ratio and depolarization ratio for the aged smoke is in
377 agreement with previous studies (e.g. Haarig et al., 2018; Hu et al., 2022 and references therein).

378

379 **30 May 2020: Urban vs Pollen**

380 Pollen grains represent a significant fraction of primary biological materials in the
381 troposphere and fluorescence induced emission provides an opportunity for their identification.
382 Fig.6 presents spatio-temporal variations of β_{532} , β_F , δ_{532} , G_F during pollen season on the night 30-
383 31 May 2020. Presence of different types of pollen over Lille in Spring – Summer 2020 was
384 discussed in our recent publication (Veselovskii et al., 2021). In particular, on 30 May 2020 the in
385 situ measurements at the roof of the building demonstrate the presence of significant amount of
386 grass pollen. The transport of pollen can be analyzed with a global-to-meso-scale dispersion model
387 SILAM (Sofiev et al., 2015). In Appendix we show the maps of the pollen index, for four sessions
388 from this study at 22 UTC. On 30 May the pollen index in Lille region is about 5.0, indicating high
389 content of pollen.

390 The aerosol is located inside the planetary boundary layer (PBL) below 2.5 km. At altitudes
391 below 1 km, the depolarization ratio δ_{532} after 23:00 increases up to ~15% simultaneously with an
392 increase of the fluorescence capacity up to 2.0×10^{-4} , which can be an indication of pollen presence.
393 On the δ_{532} - G_F diagram in Fig.7a, the single pixel data points spread from the values typical for
394 the urban particles to the values typical for the pollen. Contribution of pollen to the total
395 backscattering changes with height and the points form the pattern, similar to characteristic curve,
396 calculated for urban – pollen mixture in Fig.3. In accordance with radiosonde data from
397 Herstmonceux station, the RH at midnight was about 40% at 500 m and it increased up to 70% at
398 2000 m, thus the spatio – temporal variations of RH could influence the observed values of the
399 backscattering coefficient and depolarization ratio. In particular, the hygroscopic growth can
400 decrease the values of both δ_{532} and G_F . However, the value of the fluorescence capacity in Fig.7a
401 changes for almost one order of magnitude, and such strong change in G_F can not be explained by
402 the particle hygroscopic growth only. For example, from the recent publication of Sicard et al.
403 (2022), increase of β_{532} of urban aerosol for this range of RH, is below the factor 1.5. Thus, we
404 suppose that the pattern in Fig.7a is due to the mixing urban and pollen particles The spatio-
405 temporal distribution of aerosol types is shown in Fig.7b. The urban particles (brown) are
406 predominant, while pollen (yellow) is localized below 1 km height. The grey color corresponds to
407 unidentified aerosol type which, in our case, is the mixture of urban particles and pollen.

408 An indicator of pollen presence in an aerosol mixture, along with high depolarization ratio,
409 can be a higher value of δ_{1064} in respect to δ_{532} or δ_{355} (Cao et al., 2010; Veselovskii et al., 2021).

410 Vertical profiles of the particle depolarization ratio at all three wavelengths for this episode are
 411 given in Fig.8c of Veselovskii et al. (2021). At 0.75 km height, where δ_{1064} is about 15%, the ratio
 412 $\frac{\delta_{1064}}{\delta_{532}}$ is 1.5, which corroborates suggestions about pollen presence. For urban aerosol the
 413 depolarization spectral ratio $\frac{\delta_{1064}}{\delta_{532}}$ can be also above 1.0 (Burton et al., 2013), but absolute values
 414 of depolarization are significantly lower than for pollen particles (below 10%).

415

416 ***14 September 2020: wildfire smoke vs pollen mixture***

417 Another strong smoke episode occurred in the night 14-15 September 2020, and
 418 corresponding distributions of β_{532} , β_F , δ_{532} , and G_F are shown Fig.8. The elevated smoke layer
 419 with low depolarization ratio ($\delta_{532} < 5\%$) and high fluorescence capacity (up to 4.0×10^{-4}) was
 420 observed at approximately 6 km height during the whole night. Inside the boundary layer the
 421 depolarization ratio is higher, up to 15%, while fluorescence capacity is lower (about 1.0×10^{-4}),
 422 compared to the elevated layer. On the $\delta_{532}-G_F$ diagram in Fig.9a we can see the cluster of data
 423 points, corresponding to the smoke. The same time, a part of the points are inside the range of
 424 parameters attributed to the pollen (Table 1). The remaining points should be attributed to the
 425 mixture of pollen, smoke and urban aerosol. On the distribution of the particle types (Fig.9b) this
 426 mixture is marked with gray color. The pollen particles are localized below 1 km. Presence of
 427 pollen over Lille in September is not common, but it can be transported from other regions. The
 428 SILAM pollen index in Fig.A1 for this date demonstrates the transport of pollen to northern France
 429 from the southeast of France and the east Mediterranean.

430 Fig.10a presents profiles of δ_{532} and δ_{1064} together with β_{532} for the temporal interval 00:00
 431 – 04:00 UTC. The relative humidity, in accordance with radiosonde data from Herstmonceux
 432 station, did not exceed 50% below 1.7 km. Above that height RH increased up to 75% at 2.5 km,
 433 thus the observed increase of β_{532} above 1.5 km can be partly related to RH growth. The relative
 434 humidity inside the smoke layer did not exceed 10%. Similarly to Fig.8, δ_{1064} exceeds δ_{532} at low
 435 heights. The ratio $\frac{\delta_{1064}}{\delta_{532}}$ is about 1.5 at 1 km and inside the smoke layer $\frac{\delta_{1064}}{\delta_{532}} \approx 0.4$. Higher values
 436 of depolarization ratio at 532 nm compared to 1064 nm are reported for aged smoke by Haarig at
 437 al. (2018), Hu et al. (2019, 2022). The BAE does not present significant height variations: $A_{532/1064}^\beta$

438 is about 1.0 inside the PBL and it increases to 1.25 inside the smoke layer (Fig.10b).
439 Simultaneously, the fluorescence capacity in the smoke layer increases about a factor 4, comparing
440 to the PBL, which demonstrates efficiency of the fluorescence technique for discriminating smoke
441 from other aerosol types.

442

443 ***10 April 2020: Urban vs Pollen***

444 In the beginning of April, we experienced several atmospheric situations, for which
445 elevated layers were classified as urban aerosols. One of such cases, on the night 10 -11 April 2020,
446 is shown in Fig.11. Lidar observations were performed at an angle of 45 degrees to the horizontal,
447 so the minimum height reachable in the analysis is 350 m. The relative humidity, in accordance
448 with radiosonde data from Herstmonceux station, increased with height from 54% at 1.0 km to 65%
449 at 2.2 km. The layer with depolarization ratio δ_{532} below 5% was observed at about 2 km height
450 during the night. The fluorescence capacity in the layer is low (below 0.5×10^{-4}), so it is identified
451 as urban aerosol. HYSPLIT backward trajectories (not shown) indicate that the air masses at 750
452 m and 2000 m heights were transported from England (HYSPLIT, 2022). For the period 21:00 –
453 23:00 UTC the depolarization ratio below 500 m has increased simultaneously with the
454 fluorescence capacity, which can be an indication of pollen presence.

455 On the δ_{532} - G_F diagram (Fig.12a) the single pixel measurements in 350 m – 1500 m and
456 1500 m – 2500 m height ranges are shown by different colors. The data points related to the upper
457 layer are within the range of parameters expected for urban aerosol. The points in the lower layer
458 (below 1500 m), are partly out of this range, so the aerosol type for these points is undefined. We
459 assume that this is the mixture of urban and pollen particles, because we observe particles with
460 high depolarization ($\delta_{532} > 15\%$) and fluorescence capacity up to 0.7×10^{-4} . This mixture is marked
461 by grey color on aerosol mask in Fig.12b. The pollen index provided by SILAM over Lille on the
462 midnight, is above 4.0, so the presence of pollen particles is expectable.

463 The presence of pollen is supported also by the profiles of δ_{532} and δ_{1064} , shown in Fig.13.
464 At low heights δ_{1064} exceeds δ_{532} and the ratio $\frac{\delta_{1064}}{\delta_{532}}$ is about 1.4 at 0.5 km. However, inside the
465 elevated layer this ratio decreases and becomes about 0.8 at 2.25 km, which indicates that mixture
466 composition changed. For the same height range, the fluorescence capacity decreases from 0.6×10^{-4}

467 4 to 0.3×10^{-4} while $A_{532/1064}^\beta$ gradually increases from 0.75 to 1.25 which can be due to decrease of
468 pollen contribution.

469 As follows from Table 2, in the lower layer the values of S_{355} and S_{532} are close (about 48 ± 7
470 sr). However, in elevated layer S_{532} increases to 70 ± 7 sr, while S_{355} remains the same. Higher
471 values of S_{532} , in respect to S_{355} , are typical for aged smoke (e.g. Müller et al., 2005; Hu et al.,
472 2022). Moreover, $A_{355/532}^\beta$ significantly exceeds $A_{355/532}^\alpha$, which was also reported for aged smoke.
473 Thus, based on intensive properties only, we could classify this layer as “smoke”. However, due
474 to low fluorescence capacity, in our approach we identify it as “urban”.

475

476 ***11 August 2021: contacting layers of smoke and urban aerosol***

477 Separation of smoke and urban particles is a challenging task for Mie – Raman lidar,
478 because both types have small effective radius, and similar depolarization ratios δ_{532} . However,
479 the fluorescence capacity of smoke is about factor 4-5 higher than that of urban aerosol, which
480 allows their reliable separation. The analyses of the measurements in the night 11-12 August 2021
481 are shown in Fig.14. The RH decreases with height from 70% to 40% inside 500 m – 2250 m range.
482 The main part of aerosol is concentrated below 2500 m and two height intervals can be
483 distinguished. Above approximately 1500 m the layer with high fluorescence capacity (up to
484 3.0×10^{-4}) is observed, while in the layer below 1500 m, the G_F is low, (below 0.8×10^{-4}). HYSPLIT
485 backward trajectories (not shown) indicate that the air masses at 1800 m heights were transported
486 from North America, so these may contain wild fire smoke.

487 On the δ_{532} - G_F diagram (Fig.15a) the single pixel measurements in 500 m – 1400 m and
488 1400 m – 2500 m height ranges are shown by different colors. The cluster of points, corresponding
489 to the upper layer, is localized mainly inside the interval $1.8 \times 10^{-4} < G_F < 4.0 \times 10^{-4}$ and $4\% < \delta_{532} < 10\%$,
490 and can be attributed to smoke. The points corresponding to the lower layer are partly identified
491 as urban particles, but a part of the points is out of the range and forms a pattern typical for urban
492 – pollen mixture. The SILAM pollen index in Fig.A1 is above 5.0, so contribution of pollen can
493 be noticeable. The smoke and urban layers are in contact and the particle mixing occurs, which
494 increases dispersion within the clusters.

495 Vertical profiles of δ_{532} and $A_{532/1064}^\beta$ in Fig.16 do not demonstrate significant difference for
496 upper and lower layers. Meanwhile, the fluorescence capacity increases by factor 4. The lidar ratios

497 S_{355} and S_{532} in the upper layer, as follows from Table 2, are 45 ± 7 sr and 72 ± 11 sr respectively.
498 The $A_{355/532}^{\beta}$ significantly exceeds $A_{355/532}^{\alpha}$ (2.2 ± 0.2 and 1.0 ± 0.2 respectively), so based on
499 intensive parameters, the upper layer can be also identified as smoke.

500

501 *1 April 2021: Dust*

502 Dust layers transported from Africa are regularly observed over North of France. One such
503 dust episode took place in the night 1-2 April 2021 and the corresponding spatio-temporal
504 variations of β_{532} , β_F , δ_{532} , and G_F are shown in Fig.17. The dust layer, with depolarization ratio
505 exceeding 30%, and low fluorescence, extends from approximately 1.0 km to 5.0 km height. The
506 fluorescence capacity varied inside the layer. In the center it was the lowest (about 0.1×10^{-4}), but
507 at the bottom of the layer and near the top, G_F increased up to $(0.2\div 0.3)\times 10^{-4}$. In Fig.18a, (δ_{532} -
508 G_F diagram), we observe a cluster of particles, which can be identified as dust. There is also a
509 second small cluster, attributed to urban aerosols. On the distribution of particle types in Fig.18b
510 the urban aerosol occurs below 800 m after 23:00 UTC.

511 Fig.19 provides vertical profiles of β_{532} , δ_{532} , δ_{355} , β_F , G_F and $A_{355/532}^{\beta}$. Measurements at
512 1064 nm were not available for this episode. Depolarization ratios at 355 nm and 532 nm are close
513 to 30% through the layer, though at heights below 1.5 km there is small enhancement of δ_{532} up to
514 34%. The fluorescence capacity is about 0.4×10^{-4} at 1.5 km and it decreases with height to 0.1×10^{-4}
515 at 2.5 km. However, this decrease is not accompanied by changes in depolarization ratio. The
516 backscattering Ångstrom exponent $A_{355/532}^{\beta}$ is sensitive to the enhancement of dust absorption in
517 UV and can be negative (Veselovskii et al., 2020a). For this episode $A_{355/532}^{\beta}$ decreases with height
518 (together with G_F) to -0.3 at 2.5 km. Similar values of $A_{355/532}^{\beta}$ were observed during SHADOW
519 campaign in Western Sahara (Veselovskii et al., 2020a). Above 3.75 km both $A_{355/532}^{\beta}$ and G_F start
520 to increase. Hence, dust properties change with height and this change is not revealed on δ_{532}
521 profile. We should mention, that in publication of Veselovskii et al. (2020a), increase of the dust
522 imaginary part in UV also did not lead to changes in δ_{532} .

523 Application of our new “Fluorescence – Depolarization” based approach to six episodes
524 considered in this section, demonstrates its ability to discriminate several aerosol types. The first
525 step in validation of the results presented, could be comparison of the particle properties for

526 obtained aerosol types with corresponding values, used in existing typing algorithms. Table 3
527 provides the range of variation of particle intensive properties from publications of Burton et al.,
528 (2013), synthetic values used in NATALI algorithm (Nicolae et al., 2018) and parameters used in
529 the algorithm of Papagiannopoulos et al. (2018) for the urban, smoke and dust particles. The table
530 contains also the range of properties variation for the episodes considered in current study for the
531 same aerosol types. Parameters chosen in different algorithms, even for the same aerosol type,
532 vary in a wide range, and the values observed in this study mainly match this range of variation.
533 We observe higher values of $A_{355/532}^\beta$ for urban and smoke particles, and for dust, $A_{355/532}^\beta$ could be
534 negative. Still, the values obtained in this study and the values used by other algorithms are in
535 reasonable agreement.

536

537 **Conclusion**

538 The results presented in this study can be considered as the first important step in the
539 combination of Mie – Raman and fluorescence lidar data. In approach presented, only two
540 intensive parameters are used for classification: the particle depolarization ratio δ_{532} and the
541 fluorescence capacity G_F . These parameters are chosen because they are specific for different types
542 of aerosol and can be calculated with high spatio-temporal resolution. Moreover, δ_{532} and G_F can
543 be calculated at lower altitudes, compared to extinction related parameters, such as lidar ratio and
544 extinction Angstrom exponent. Thus classification, in principle, is possible at ranges with
545 incomplete geometrical overlap. Finally, computation of β_F does not demand the use of reference
546 height, only calibration of relative sensitivity of the channels is needed. Thus, aerosol classification
547 is possible, even in the presence of low-level clouds.

548 Though only two aerosol properties are considered, the use of fluorescence provides
549 advances in aerosol classification. Analysis of numerous observations, performed at Lille
550 University for the period 2020 – 2021, demonstrates the possibility to separate four types of
551 aerosols, such as dust, smoke, pollen and urban. Moreover, we are able to identify the layers
552 containing the liquid water particles and ice. The number of determined aerosol classes can be
553 increased, by considering the particle mixtures. In particular, “pure” dust can be considered
554 separately from “polluted” one, which can be discriminated by lower values of the depolarization
555 ratio.

556 Fluorescence technique is especially promising for separation of smoke and urban particles,
557 because fluorescence capacity of smoke is about factor five higher. The important advantage of
558 fluorescence measurements is the ability to identify the biological particles in the atmosphere, such
559 as pollen, which are usually not included in the classification schemes, based on Mie-Raman
560 observations. At the same time, our observations demonstrate that biological particles are
561 frequently observed during Spring – Autumn seasons and may contribute significantly to the
562 aerosol composition inside the PBL. The developed approach allows to identify aerosol types with
563 high spatio-temporal resolutions, which is estimated to be 60 m for height and less than 10 minutes
564 for time, for the current instrumental configuration. Such resolution provides an opportunity for
565 investigating the dynamics of aerosol mixing in the troposphere.

566 The next step in algorithm development will be to include additional particle properties.
567 We plan to include the backscattering Angstrom exponents and the depolarization spectral ratios
568 ($\delta_{355}/\delta_{532}$ and $\delta_{532}/\delta_{1064}$), which can be also calculated with high spatio-temporal resolutions. The
569 fluorescence capacity depends on the relative humidity, due to the effects of hygroscopic growth.
570 Thus, information about spatio-temporal distribution of RH should be included in the analysis. It
571 is also important to combine our algorithm with existing classification schemes, which we plan to
572 consider in the near future.

573

574 **Data availability.** Lidar measurements are available upon request
575 (philippe.goloub@univ-lille.fr).

576

577 **Author contributions.** IV processed the data and wrote the paper. QH and TP performed the
578 measurements. PG supervised the project and helped with paper preparation. BB prepared
579 algorithm for aerosol classification. MK developed software for data processing.

580 .

581 **Competing interests.** The authors declare that they have no conflict of interests.

582

583 **Acknowledgement**

584 We acknowledge funding from the CaPPA project funded by the ANR through the PIA under
585 contract [ANR-11-LABX-0005-01](#), the “Hauts de France” Regional Council (project CLIMIBIO)
586 and the European Regional Development Fund (FEDER). ESA/QA4EO program is greatly
587 acknowledged for support of observation activity at LOA as well as OBS4CLIM Equipex project
588 funded by ANR. Development of algorithm for aerosol typing was supported by Russian Science

589 Foundation (project 21-17-00114). The SILAM model is acknowledged for providing pollen
590 simulations.

591

592 **References**

593 Adam, M., Stachlewska, I. S., Mona, L., Papagiannopoulos, N., Bravo-Aranda, J. A., Sicard, M.,
594 Nicolae, D. N., Belegante, L., Janicka, L., Szczepanik, D., Mylonaki, M., Papanikolaou, C.-A.,
595 Siomos, N., Voudouri, K. A., Alados-Arboledas, L., Apituley, A., Mattis, I., Chaikovsky, A.,
596 Muñoz-Porcar, C., Pietruczuk, A., Bortoli, D., Baars, H., Grigorov, I., and Peshev, Z.: Biomass
597 burning events measured by lidars in EARLINET – Part 2: Optical properties investigation,
598 *Atmos. Chem. Phys. Discuss.*, <https://doi.org/10.5194/acp-2021-759>, in review, 2021.

599 Ansmann, A., Riebesell, M., Wandinger, U., Weitkamp, C., Voss, E., Lahmann, W., and
600 Michaelis, W.: Combined Raman elastic-backscatter lidar for vertical profiling of moisture,
601 aerosols extinction, backscatter, and lidar ratio, *Appl.Phys.B*, 55, 18-28, 1992.

602 Bohlmann, S., Shang, X., Giannakaki, E., Filioglou, M., Saarto, A., Romakkaniemi, S. and
603 Komppula, M.: Detection and characterization of birch pollen in the atmosphere using multi-
604 wavelength Raman lidar in Finland, *Atmos. Chem. Phys.* 19, 14559–14569, 2019.
605 doi.org/10.5194/acp-19-14559-2019.

606 Boucher, O., Randall, D., Artaxo, P., Bretherton, C., Feingold, G., Forster, P., Kerminen, V.-M.,
607 Kondo, Y., Liao, H., Lohmann, U., Rasch, P., Satheesh, S. K., Sherwood, S., Stevens, B., and
608 Zhang, X. Y.: Clouds and Aerosols, in: *Climate Change 2013: The Physical Science Basis*.
609 Contribution of Working Group I to the Fifth Assessment Report of the Intergovernmental Panel
610 on Climate Change, edited by: Stocker, T. F., Qin, D., Plattner, G.-K., Tignor, M., Allen, S. K.,
611 Boschung, J., Nauels, A., Xia, Y., Bex, V., and Midgley, P., M., Cambridge University Press,
612 Cambridge, United Kingdom and New York, NY, USA, 2013

613 Burton, S. P., Ferrare, R. A., Hostetler, C. A., Hair, J.W., Rogers, R. R., Obland, M. D., Butler, C.
614 F., Cook, A. L., Harper, D. B., and Froyd, K. D.: Aerosol classification using airborne High
615 Spectral Resolution Lidar measurements – methodology and examples, *Atmos. Meas. Tech.*, 5,
616 73–98, 2012. <https://doi.org/10.5194/amt-5-73-2012>

617 Burton, S. P., Ferrare, R. A., Vaughan, M. A., Omar, A. H., Rogers, R. R., Hostetler, C. A., and
618 Hair, J. W.: Aerosol classification from airborne HSRL and comparisons with the CALIPSO

619 vertical feature mask, *Atmos. Meas. Tech.*, 6, 1397–1412, 2013. [https://doi.org/10.5194/amt-6-](https://doi.org/10.5194/amt-6-1397-2013)
620 1397-2013

621 Burton, S. P., Vaughan, M. A., Ferrare, R. A. and Hostetler, C. A.: Separating mixtures of
622 aerosol types in airborne High Spectral Resolution Lidar data. *Atmos. Meas. Tech.* 7, 419-
623 436, 2014. DOI: 10.5194/amt-7-419-2014

624 Burton, S. P., Hair, J. W., Kahnert, M., Ferrare, R. A., Hostetler, C. A., Cook, A. L., Harper, D.
625 B., Berkoff, T. A., Seaman, S. T., Collins, J. E., Fenn, M. A., and Rogers, R. R.: Observations
626 of the spectral dependence of linear particle depolarization ratio of aerosols using NASA
627 Langley airborne High Spectral Resolution Lidar, *Atmos. Chem. Phys.*, 15, 13453–13473, 2015
628 doi:10.5194/acp-15-13453-2015

629 Cao, X., Roy, G., and Bernier, R.: Lidar polarization discrimination of bioaerosols, *Opt. Eng.*, 49,
630 116201, <https://doi.org/10.1117/1.3505877>, 2010.

631 Dubovik, O., Holben, B. N., Eck, T. F., Smirnov, A., Kaufman, Y. J., King, M. D., Tanre, D., and
632 Slutsker, I.: Variability of absorption and optical properties of key aerosol types observed in
633 worldwide locations, *J. Atmos. Sci.*, 59, 590–608, 2002.

634 Freudenthaler, V., Esselborn, M., Wiegner, M., Heese, B., Tesche, M. and co-authors:
635 Depolarization ratio profiling at several wavelengths in pure Saharan dust during SAMUM
636 2006, *Tellus* 61B, 165–179, 2009.

637 Gasteiger, J. and Freudenthaler, V.: Benefit of depolarization ratio at $\lambda = 1064$ nm for the
638 retrieval of the aerosol microphysics from lidar measurements. *Atmos. Meas. Tech.* 7, 3773-
639 3781, 2014. DOI: 10.5194/amt-7-3773-2014

640 Giles, D. M., Holben, B. N., Eck, T. F., Sinyuk, A., Smirnov, A., Slutsker, I., Dickerson, R. R.,
641 Thompson, A. M., and Schafer, J. S.: An analysis of AERONET aerosol absorption properties
642 and classifications representative of aerosol source regions, *J. Geophys. Res.* 117, D17203,
643 <https://doi.org/10.1029/2012JD018127>, 2012.

644 Groß, S., Tesche, M., Freudenthaler, V., Toledano, C., Wiegner, M., Ansmann, A., Althausen D.,
645 Seefeldner, M.: Characterization of Saharan dust, marine aerosols and mixtures of biomass-
646 burning aerosols and dust by means of multi-wavelength depolarization and Raman lidar
647 measurements during SAMUM 2. *Tellus B* 63, 706-724, 2011. DOI: 10.1111/j.1600-
648 0889.2011.00556.

649 Groß, S., Esselborn, M., Weinzierl, B., Wirth, M., Fix, A., and Petzold, A.: Aerosol classification
650 by airborne high spectral resolution lidar observations, *Atmos. Chem. Phys.*, 13, 2487–2505,
651 2013. <https://doi.org/10.5194/acp-13-2487-2013>

652 Haarig, M., Ansmann, A., Baars, H., Jimenez, C., Veselovskii, I., Engelmann, R., and Althausen,
653 D.: Depolarization and lidar ratios at 355, 532, and 1064 nm and microphysical properties of
654 aged tropospheric and stratospheric Canadian wildfire smoke, *Atmospheric Chemistry and
655 Physics*, 18, 11 847–11 861, 2018.

656 Hamill, P., Giordano, M., Ward, C., Giles, D., and Holben, B.: An AERONET-based aerosol
657 classification using the Mahalanobis distance, *Atmos. Environ.*, 140, 213–233,
658 <https://doi.org/10.1016/j.atmosenv.2016.06.002>, 2016.

659 Hara, Y., Nishizawa, T., Sugimoto, N., Osada, K., Yumimoto, K., Uno, I., Kudo, R., and Ishimoto,
660 H.: Retrieval of aerosol components using multi-wavelength Mie-Raman lidar and comparison
661 with ground aerosol sampling, *Remote Sens.*, 10, 937, 2018. <https://doi.org/10.3390/rs10060937>

662 Hu, Q., Goloub, P., Veselovskii, I., Bravo-Aranda, J.-A., Popovici, I. E., Podvin, T., Haeffelin,
663 M., Lopatin, A., Dubovik, O., Pietras, C., et al.: Long-range-transported Canadian smoke
664 plumes in the lower stratosphere over northern France, *Atmospheric Chemistry and Physics*,
665 19, 1173–1193, 2019.

666 Hu, Q., Goloub, P., Veselovskii, I., and Podvin, T.: The characterization of long-range transported
667 North American biomass burning plumes: what can a multi-wavelength Mie-Raman-
668 polarization-fluorescence lidar provide?, *Atmos. Chem. Phys.*, 22, 5399–5414, 2022
669 <https://doi.org/10.5194/acp-22-5399-2022>

670 HYSPLIT(2022): HYbrid Single-Particle Lagrangian Integrated Trajectory model, backward
671 trajectory calculation tool, available at: http://ready.arl.noaa.gov/HYSPLIT_traj.php, last
672 access: 14 June 2022.

673 Klett J.D., “Lidar inversion with variable backscatter/extinction ratios”, *Appl.Opt.* 24, 1638-1643,
674 1985.

675 Li, L., Dubovik, O., Derimian, Y., Schuster, G. L., Lapyonok, T., Litvinov, P., Ducos, F., Fuertes,
676 D., Chen, C., Li, Z., Lopatin, A., Torres, B., and Che, H.: Retrieval of aerosol components
677 directly from satellite and ground-based measurements, *Atmos. Chem. Phys.*, 19, 13409–13443,
678 2019. <https://doi.org/10.5194/acp-19-13409-2019>

679 Mamouri, R.-E., and Ansmann, A.: Potential of polarization/Raman lidar to separate fine dust,
680 coarse dust, maritime, and anthropogenic aerosol profiles, *Atmos. Meas. Tech.*, 10, 3403–3427,
681 2017. <https://doi.org/10.5194/amt-10-3403-2017>

682 Müller, D., Mattis, I., Wandinger, U., Ansmann, A., Althausen, A., and Stohl, A.: Raman lidar
683 observations of aged Siberian and Canadian forest fire smoke in the free troposphere over
684 Germany in 2003: Microphysical particle characterization, *J. Geophys. Res.*, 110, D17201,
685 doi:10.1029/2004JD005756, 2005.

686 Mylonaki, M., Giannakaki, E., Papayannis, A., Papanikolaou, C.-A., Komppula, M., Nicolae, D.,
687 Papagiannopoulos, N., Amodeo, A., Baars, H., and Soupiona, O.: Aerosol type classification
688 analysis using EARLINET multiwavelength and depolarization lidar observations, *Atmos.*
689 *Chem. Phys.*, 21, 2211–2227, 2021. <https://doi.org/10.5194/acp-21-2211-2021>

690 Nicolae, D., Vasilescu, J., Talianu, C., Biniotoglou, I., Nicolae, V., Andrei, S., and Antonescu, B.:
691 A neural network aerosol-typing algorithm based on lidar data, *Atmos. Chem. Phys.*, 18,
692 14511–14537, 2018. <https://doi.org/10.5194/acp-18-14511-2018>

693 Papagiannopoulos, N., Mona, L., Amodeo, A., D’Amico, G., Gumà Claramunt, P., Pappalardo, G.,
694 Alados-Arboledas, L., Guerrero-Rascado, J. L., Amiridis, V., Kokkalis, P., Apituley, A., Baars,
695 H., Schwarz, A., Wandinger, U., Biniotoglou, I., Nicolae, D., Bortoli, D., Comerón, A.,
696 Rodríguez-Gómez, A., Sicard, M., Papayannis, A., and Wiegner, M.: An automatic observation-
697 based aerosol typing method for EARLINET, *Atmos. Chem. Phys.*, 18, 15879–15901, 2018.
698 <https://doi.org/10.5194/acp-18-15879-2018>

699 Pappalardo, G., Amodeo, A., Apituley, A., Comeron, A., Freudenthaler, V., Linné, H., Ansmann,
700 A., Bösenberg, J., D’Amico, G., Mattis, I., Mona, L., Wandinger, U., Amiridis, V., Alados-
701 Arboledas, L., Nicolae, D., and Wiegner, M.: EARLINET: towards an advanced sustainable
702 European aerosol lidar network, *Atmos. Meas. Tech.*, 7, 2389–2409, 2014.
703 <https://doi.org/10.5194/amt-7-2389-2014>, 2014.

704 Reichardt, J., Leinweber, R., Schwebe, A.: Fluorescing aerosols and clouds: investigations of co-
705 existence, Proceedings of the 28th ILRC, Bucharest, Romania, 25-30 June, 2017.

706 Rittmeister, F., Ansmann, A., Engelmann, R., Skupin, A., Baars, H., Kanitz, T., and Kinne, S.:
707 Profiling of Saharan dust from the Caribbean to western Africa –Part 1: Layering structures and
708 optical properties from shipborne polarization/Raman lidar observations, *Atmos. Chem. Phys.*,
709 17, 12963–12983, 2017. <https://doi.org/10.5194/acp-17-12963-2017>

710 Saito, Y., Hosokawa, T., Shiraishi, K.: Collection of excitation-emission-matrix fluorescence of
711 aerosol-candidate-substances and its application to fluorescence lidar monitoring, *Appl. Opt.*,
712 61, 653 – 660, 2022.

713 Schuster, G. L., Dubovik, O., and Arola, A.: Remote sensing of soot carbon – Part 1:
714 Distinguishing different absorbing aerosol species, *Atmos. Chem. Phys.*, 16, 1565–1585,
715 <https://doi.org/10.5194/acp-16-1565-2016>, 2016.

716 Sicard, M., Fortunato dos Santos Oliveira, D. C., Muñoz-Porcar, C., Gil-Díaz, C., Comerón, A.,
717 Rodríguez-Gómez, A., and Dios Otín, F.: Measurement Report: Spectral and statistical analysis
718 of aerosol hygroscopic growth from multi-wavelength lidar measurements in Barcelona, Spain,
719 *Atmos. Chem. Phys.* 22, 7681–7697, 2022. <https://doi.org/10.5194/acp-22-7681-2022>

720 Sofiev, M., Siljamo, P., Ranta, H., Linkosalo, T., Jaeger, S., Rasmussen, A., Rantio-Lehtimäki, A.,
721 Severova, E., Kukkonen, J. (2012) A numerical model of birch pollen emission and dispersion
722 in the atmosphere. Description of the emission module. *Int. J. Biometeorology*,
723 <http://www.ncbi.nlm.nih.gov/pubmed/22410824>, DOI 10.1007/s00484-012-0532-z, PMID
724 22410824

725 Sofiev, M., Vira, J., Kouznetsov, R., Prank, M., Soares, J., Genikhovich, E. (2015) Construction
726 of the SILAM Eulerian atmospheric dispersion model based on the advection algorithm of
727 Michael Galperin, *Geosci. Model Developm.* 8, 3497–3522, doi:10.5194/gmd-8-3497-2015

728 Sofiev, M. On impact of transport conditions on variability of the seasonal pollen index.
729 *Aerobiologia* 33, 167–179 (2017). <https://doi.org/10.1007/s10453-016-9459-x>

730 Sugimoto, N. and Lee, C. H.: Characteristics of dust aerosols inferred from lidar depolarization
731 measurements at two wavelengths. *Applied Optics* 45, 7468–7474, 2006. DOI:
732 10.1364/AO.45.007468

733 Sugimoto, N., Huang, Z., Nishizawa, T., Matsui, I., Tatarov, B.: Fluorescence from atmospheric
734 aerosols observed with a multichannel lidar spectrometer," *Opt. Expr.* 20, 20800–20807, 2012.

735 Tesche, M., Ansmann, A., Müller, D., Althausen, D., Mattis, I., Heese, B., Freudenthaler, V.,
736 Wiegner, M., Eeseborn, M., Pisani, G., and Knippertz, P.: Vertical profiling of Saharan dust
737 with Raman lidars and airborne HSRL in southern Morocco during SAMUM, *Tellus B*, 61,
738 144–164, 2009.

739 Veselovskii, I., Whiteman, D. N., Korenskiy, M., Suvorina, A., Perez-Ramirez, D.: Use of
740 rotational Raman measurements in multiwavelength aerosol lidar for evaluation of particle
741 backscattering and extinction, *Atmos. Meas. Tech.*, 8, 4111–4122, 2015.

742 Veselovskii, I., Hu, Q., Goloub, P., Podvin, T., Korenskiy, M., Derimian, Y., Legrand, M., and
743 Castellanos, P.: Variability in lidar-derived particle properties over West Africa due to changes
744 in absorption: towards an understanding, *Atmos. Chem. Phys.*, 20, 6563–6581, 2020a.
745 <https://doi.org/10.5194/acp-20-6563-2020a>

746 Veselovskii, I., Hu, Q., Goloub, P., Podvin, T., Korenskiy, M., Pujol, O., Dubovik, O., Lopatin,
747 A.: Combined use of Mie-Raman and fluorescence lidar observations for improving aerosol
748 characterization: feasibility experiment, *Atm. Meas. Tech.*, 13, 6691–6701, 2020b.
749 doi.org/10.5194/amt-13-6691-2020.

750 Veselovskii, I., Hu, Q., Goloub, P., Podvin, T., Choël, M., Visez, N., and Korenskiy, M.: Mie–
751 Raman–fluorescence lidar observations of aerosols during pollen season in the north of France,
752 *Atm. Meas. Tech.*, 14, 4773–4786, 2021. doi.org/10.5194/amt-14-4773-2021

753 Veselovskii, I., Hu, Q., Ansmann, A., Goloub, P., Podvin, T., Korenskiy, N.: Fluorescence lidar
754 observations of wildfire smoke inside cirrus: A contribution to smoke-cirrus - interaction
755 research, *Atmos. Chem. Phys.* 22, 5209–5221, 2022. <https://doi.org/10.5194/acp-22-5209-2022>

756 Voudouri, K. A., Siomos, N., Michailidis, K., Papagiannopoulos, N., Mona, L., Cornacchia, C.,
757 Nicolae, D., and Balis, D.: Comparison of two automated aerosol typing methods and their
758 application to an EARLINET station, *Atmos. Chem. Phys.*, 19, 10961–10980, 2019.
759 <https://doi.org/10.5194/acp-19-10961-2019>

760 Wang, N., Shen, X., Xiao, D., Veselovskii, I., Zhao, C., Chen, F., Liu, C., Rong, Y., Ke, J., Wang,
761 B., Qi, B., Liu, D.: Development of ZJU high-spectral-resolution lidar for aerosol and cloud:
762 feature detection and classification, *Journal of Quantitative Spectroscopy & Radiative Transfer*,
763 v.261, 107513, 2021. doi.org/10.1016/j.jqsrt.2021.107513

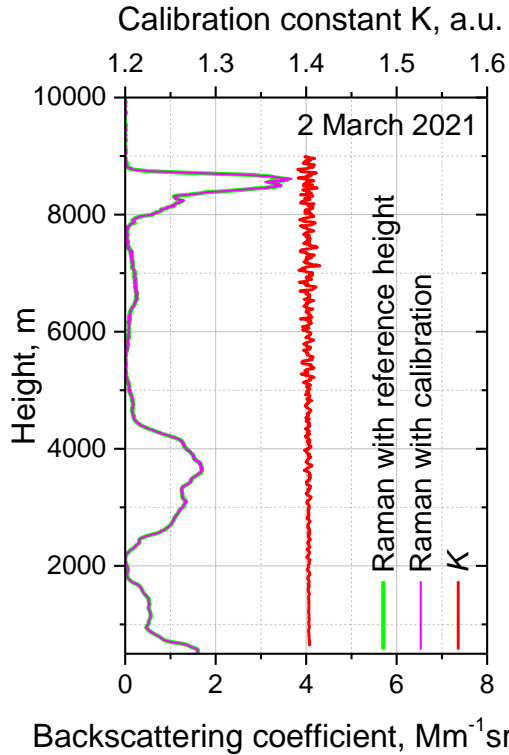
764 Whiteman, D.N.: Examination of the traditional Raman lidar technique. II. Evaluating the ratios
765 for water vapor and aerosols, *Appl. Opt.*, 42, 2593-2608, 2003.
766 <https://doi.org/10.1364/AO.42.002593>

767 Zhang, Y., Li, Z., Chen, Y., Leeuw, G., Zhang, C., Xie, Y., and Li, K.: Improved inversion of
768 aerosol components in the atmospheric column from remote sensing data, *Atmos. Chem. Phys.*,
769 20, 12795–12811, 2020. <https://doi.org/10.5194/acp-20-12795-2020>

770 Zhang, Y., Sun, Z., Chen, S., Chen, H., Guo, P., Chen, S., He, J., Wang, J., Nian, X.: Classification
771 and source analysis of low-altitude aerosols in Beijing using fluorescence–Mie polarization
772 lidar, *Optics Communications*, 479, 126417, 2021.
773 <https://doi.org/10.1016/j.optcom.2020.126417>
774
775

776

777



778

779

780

781

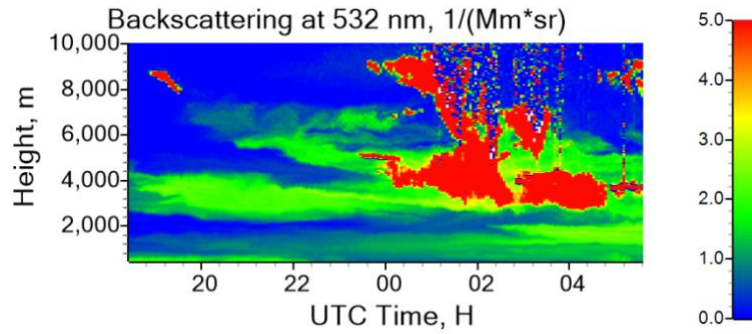
782

783

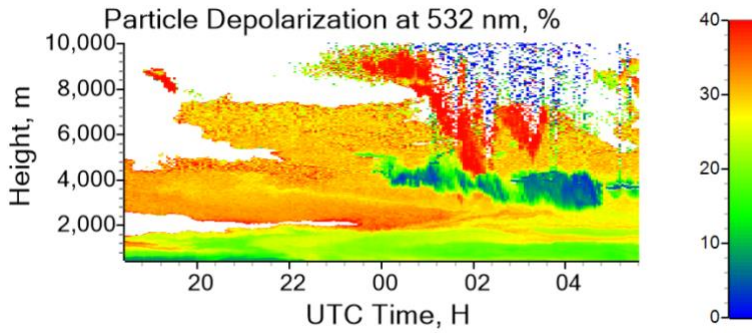
784

Fig.1. Backscattering coefficients at 532 nm for period 19:00 – 20:00 UTC on 2 March 2021 calculated from Mie-Raman observations using the reference height as Ansmann et al. (1992) (green) or the calibration constant as in Eq 5. (magenta). The profile of calibration constant K is shown with red line.

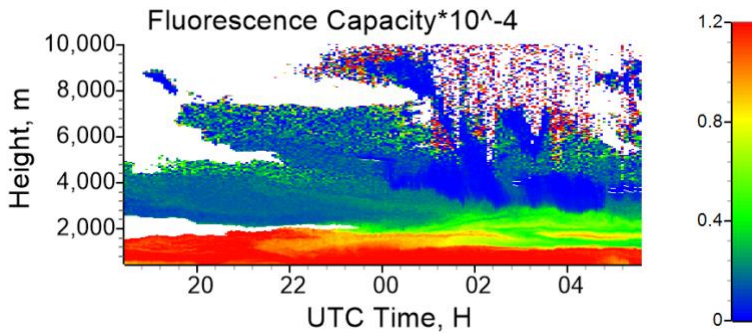
785
786



787

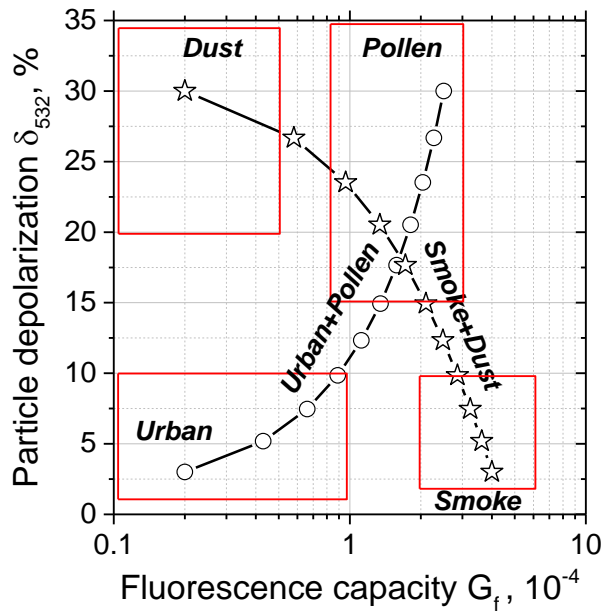


788



789

790 Fig.2. Spatio-temporal distributions of the backscattering coefficient β_{532} , the particle
791 depolarization ratio δ_{532} and the fluorescence capacity G_F in the night 2-3 March 2021. The
792 backscattering coefficient β_{532} is calculated with the modified Raman method. The values of δ_{532} ,
793 and G_F are shown for $\beta_{532} > 0.2 \text{ Mm}^{-1} \text{sr}^{-1}$.
794

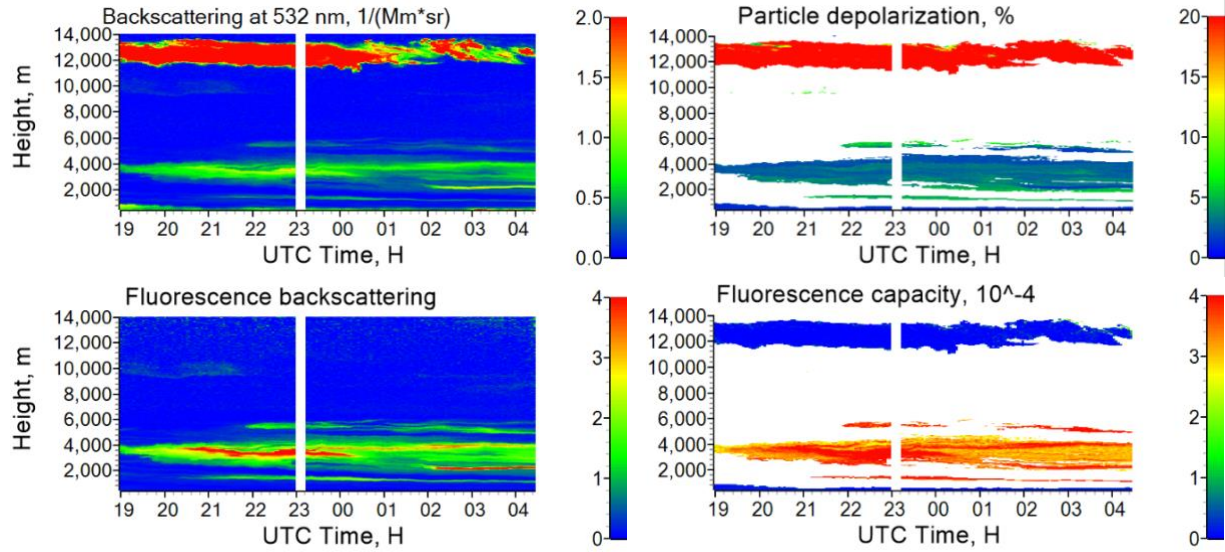


796

797 Fig.3. Aerosol typing with δ_{532} - G_F diagram. The ranges of the particle parameters variation for
 798 dust, pollen, smoke and urban aerosol are given by rectangles. The symbols show the results of
 799 simulation performed for pollen+urban (circles) and smoke + dust (stars) mixtures. Relative
 800 contribution of pollen (smoke) to the total backscattering β_{532} varied in 0 – 1.0 range with step 0.1.
 801 Particle parameters used in calculations are given in the text.

802

803

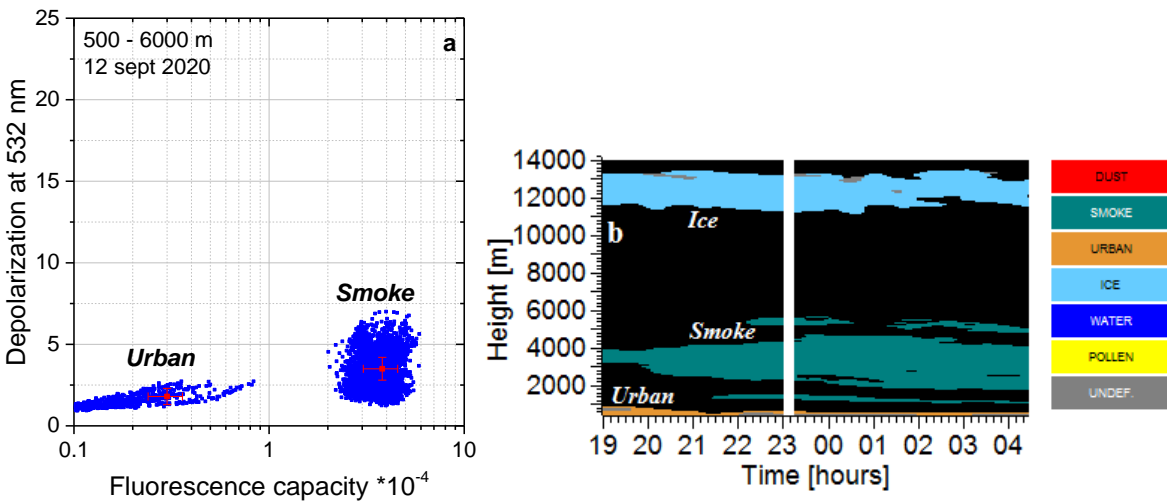


804

805

806

807 Fig.4. Spatio-temporal distributions of the backscattering coefficient β_{532} , the fluorescence
 808 backscattering coefficient β_F (in $10^{-4} \text{ Mm}^{-1}\text{sr}^{-1}$), the particle depolarization ratio δ_{532} ; and the
 809 fluorescence capacity G_F in the night 12-13 September 2020. Calculation of δ_{532} and G_F was not
 810 performed for $\beta_{532} < 0.2 \text{ Mm}^{-1}\text{sr}^{-1}$.
 811

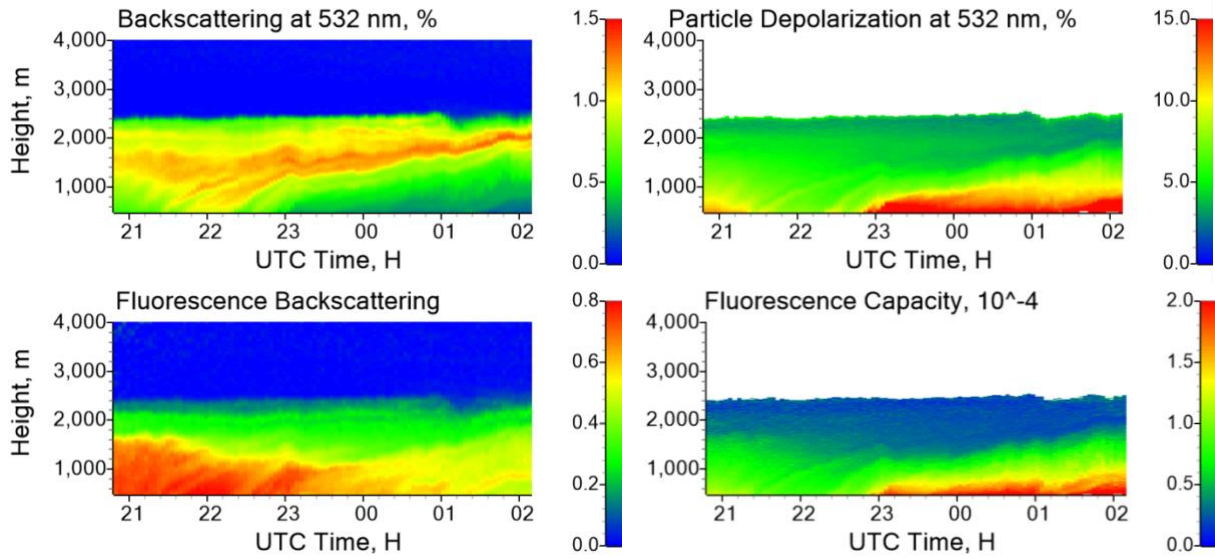


812

813 Fig.5 (a) The δ_{532} - G_F diagram for data from Fig.4 in 500 – 6000 m height range, red crosses show
 814 the uncertainty of the measurements. (b) Spatio-temporal distribution of aerosol types in the night
 815 12-13 September 2020. Grey color shows undefined aerosol type, while measurements with
 816 $\beta_{532} < 0.2 \text{ Mm}^{-1}\text{sr}^{-1}$ are marked by black color.
 817

818

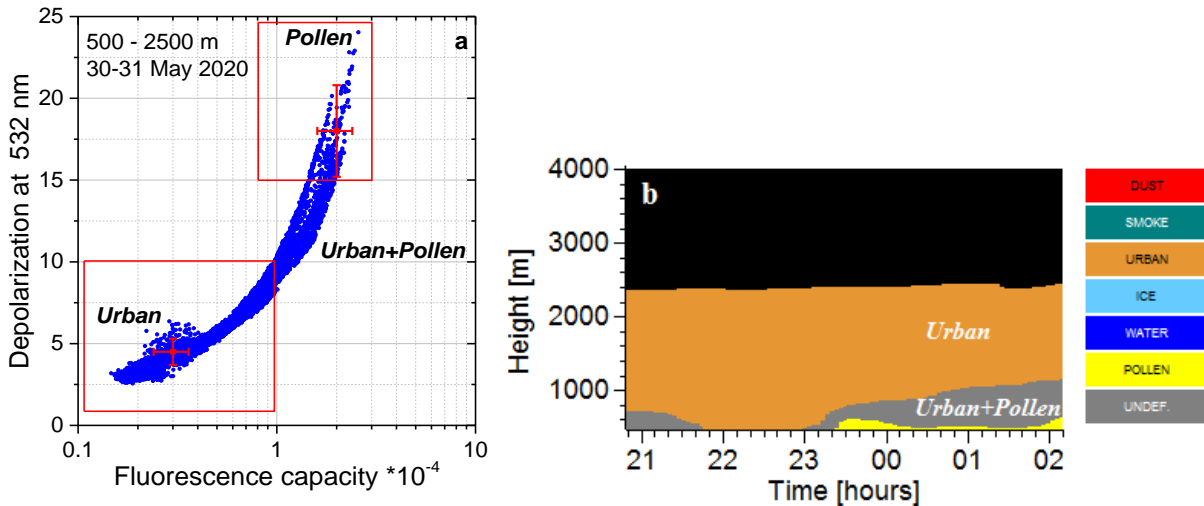
819
820



821

822
823
824
825
826

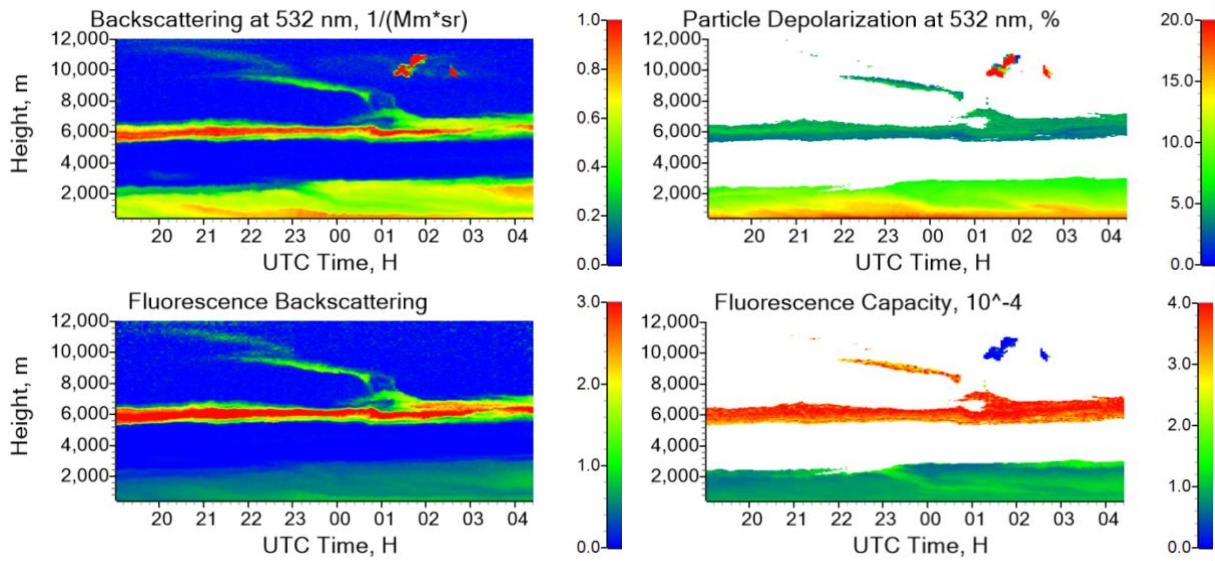
Fig.6. Spatio-temporal distributions of the backscattering coefficient β_{532} ; the fluorescence backscattering coefficient β_F (in $10^{-4} \text{ Mm}^{-1}\text{sr}^{-1}$); the particle depolarization ratio δ_{532} ; and the fluorescence capacity G_F in the night 30-31 May 2020.



827
828
829
830
831
832

Fig.7. (a) The δ_{532} - G_F diagram for observations in 500 m – 2500 m height range and (b) spatio-temporal distribution of aerosol types on the night 30-31 May 2020. Grey color shows undefined aerosol type, which is a mixture of urban and pollen for this case. Measurements with $\beta_{532} < 0.2 \text{ Mm}^{-1}\text{sr}^{-1}$ are marked by black color.

833

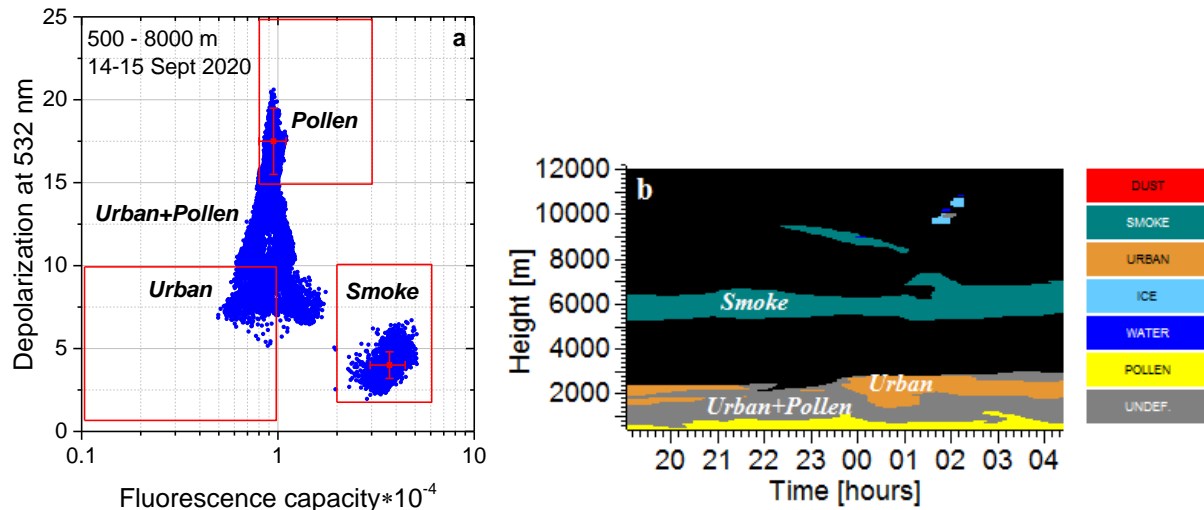


834

835

836 Fig.8. Spatio-temporal distributions of the backscattering coefficient β_{532} , the fluorescence
 837 backscattering coefficient β_F (in $10^{-4} \text{ Mm}^{-1}\text{sr}^{-1}$), the particle depolarization ratio δ_{532} , and the
 838 fluorescence capacity G_F in the night 14 – 15 September 2020. Measurements with $\beta_{532} < 0.2 \text{ Mm}^{-1}$
 839 sr^{-1} are marked by black color.

840



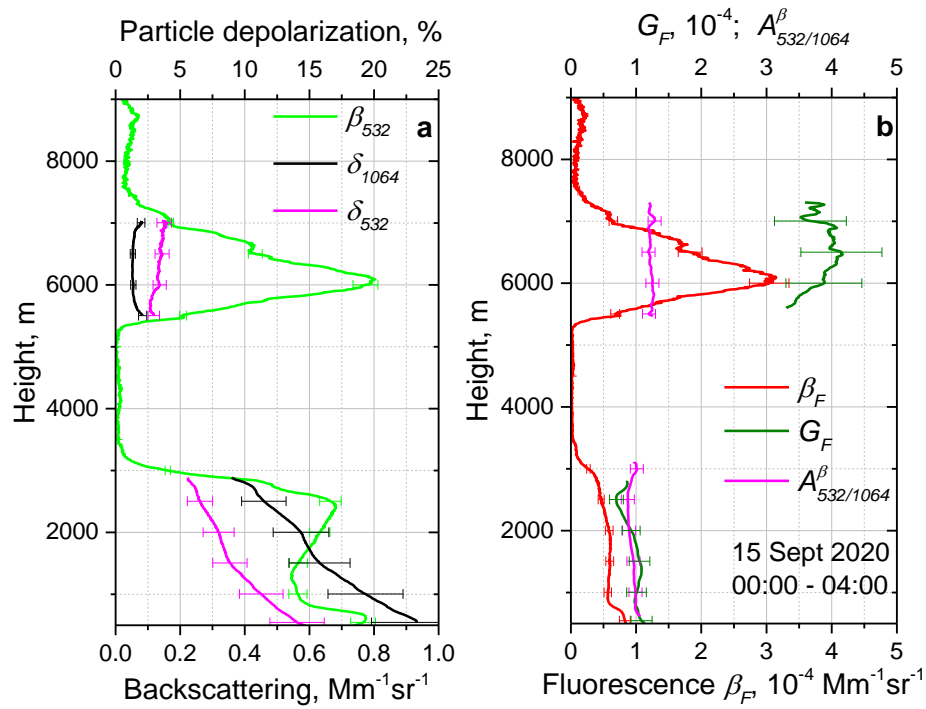
841

842 Fig.9. (a) The δ_{532} - G_F diagram for observations in 500 m – 8000 m height range and (b) spatio-
 843 temporal distribution of aerosol types in the night 14 – 15 September 2020. Grey color shows
 844 undefined aerosol type, which is a mixture of pollen, urban and smoke particles.

845

846

847



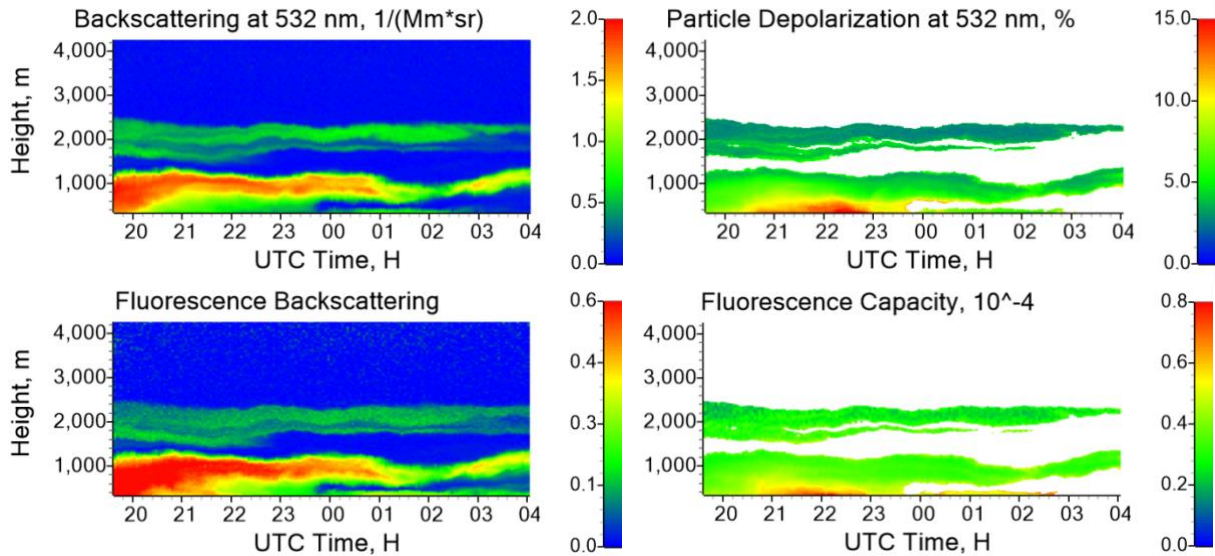
849

850 Fig.10. Vertical profiles of (a) backscattering coefficient β_{532} and particle depolarization ratios δ_{532} ,851 δ_{1064} ; (b) fluorescence backscattering β_F , fluorescence capacity G_F and backscattering Angstrom852 exponent $A_{532/1064}^\beta$ on 15 September 2020 for period 00:00 – 04:00 UTC.

853

854

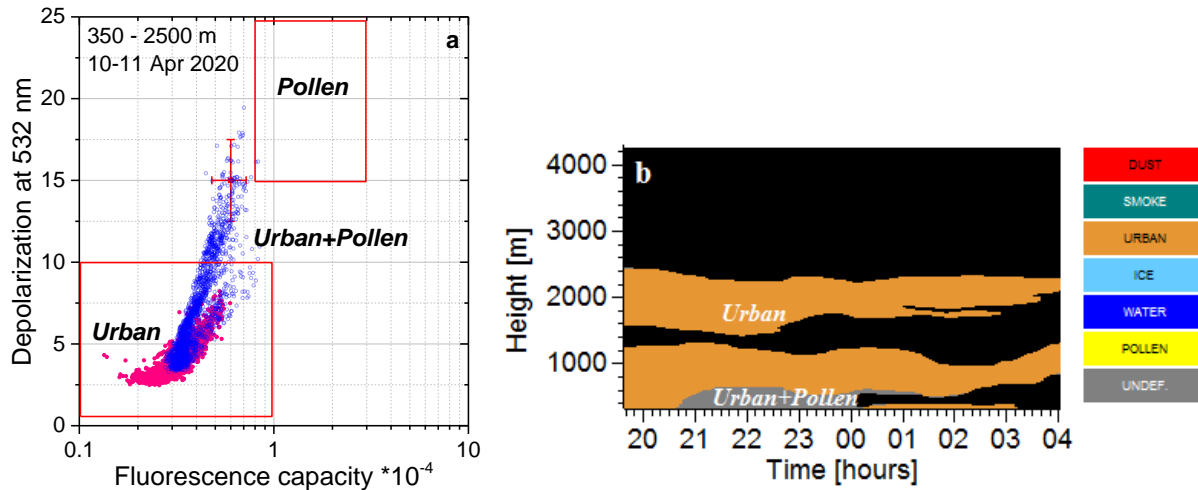
855



856

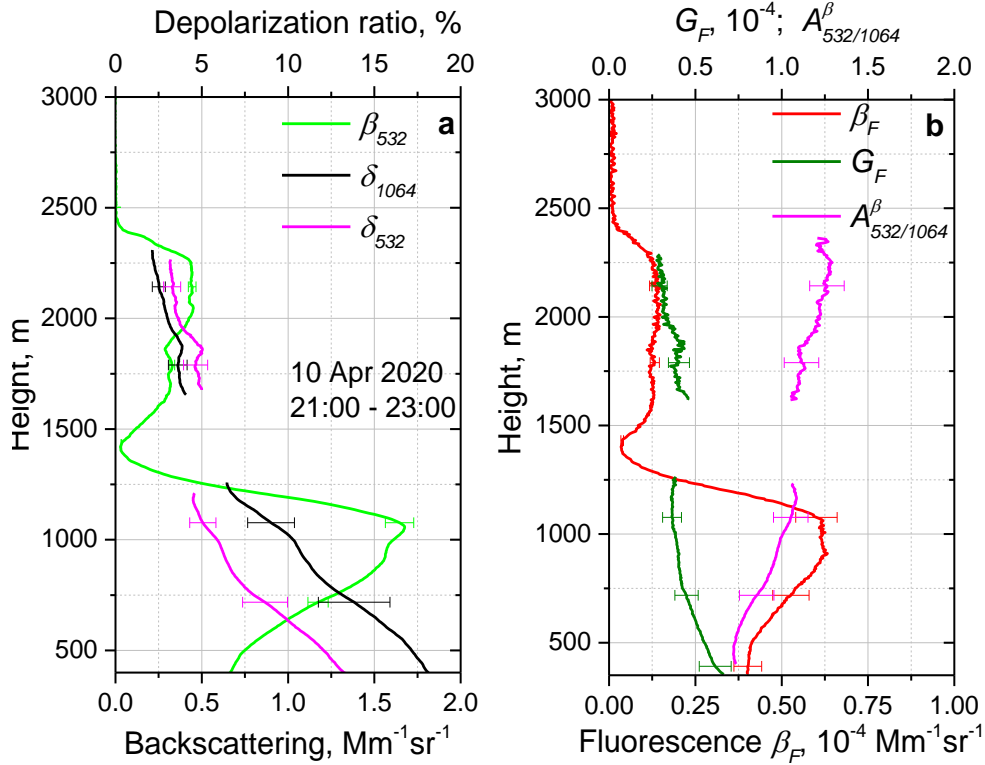
857

858 Fig.11. Spatio-temporal distributions of the backscattering coefficient β_{532} , the fluorescence
 859 backscattering coefficient β_F (in $10^{-4} Mm^{-1}sr^{-1}$), the particle depolarization ratio δ_{532} ; and the
 860 fluorescence capacity G_F in the night 10 – 11 April 2020. Measurements are performed at an angle
 861 of 45 dg to horizon.
 862



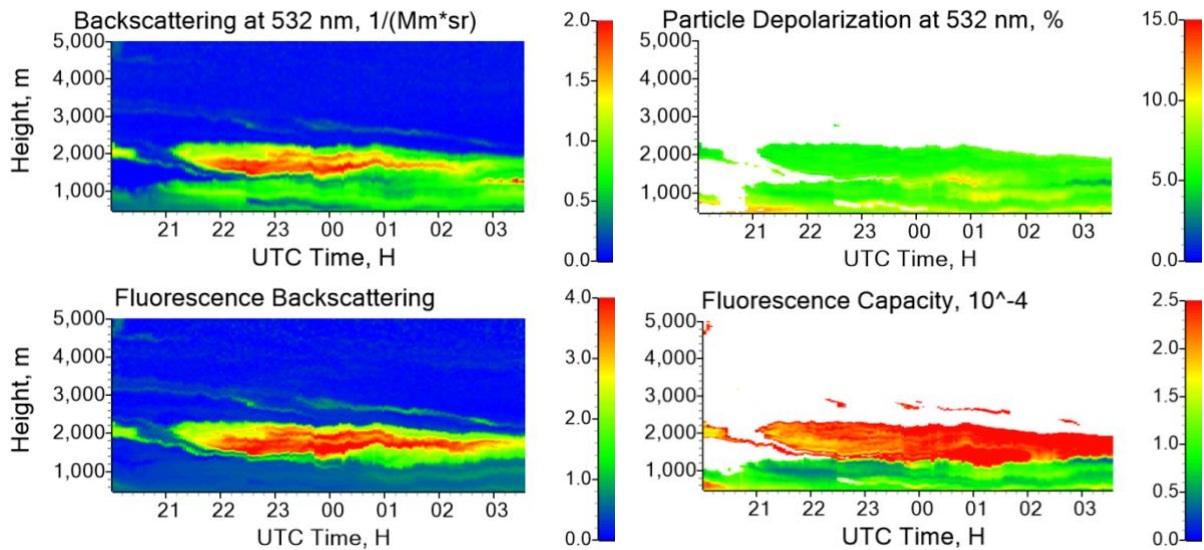
863

864 Fig.12. (a) The δ_{532} - G_F diagram for observations in 350 – 1500 m (blue symbols) and 1500 – 2500
 865 m (pink symbols) height ranges. (b) Spatio-temporal distribution of aerosol types in the night 10
 866 – 11 April 2020. Grey color shows undefined aerosol type, which is a mixture of urban and pollen
 867 for this case. Measurements with $\beta_{532} < 0.2 Mm^{-1}sr^{-1}$ are marked by black color.
 868



869
 870 Fig.13. Vertical profiles of (a) backscattering coefficient β_{532} and particle depolarization ratios δ_{532} ,
 871 δ_{1064} ; (b) fluorescence backscattering β_F , fluorescence capacity G_F and backscattering Angstrom
 872 exponent $A_{532/1064}^\beta$ on 10 April 2020 for period 21:00 – 23:00 UTC.
 873

874

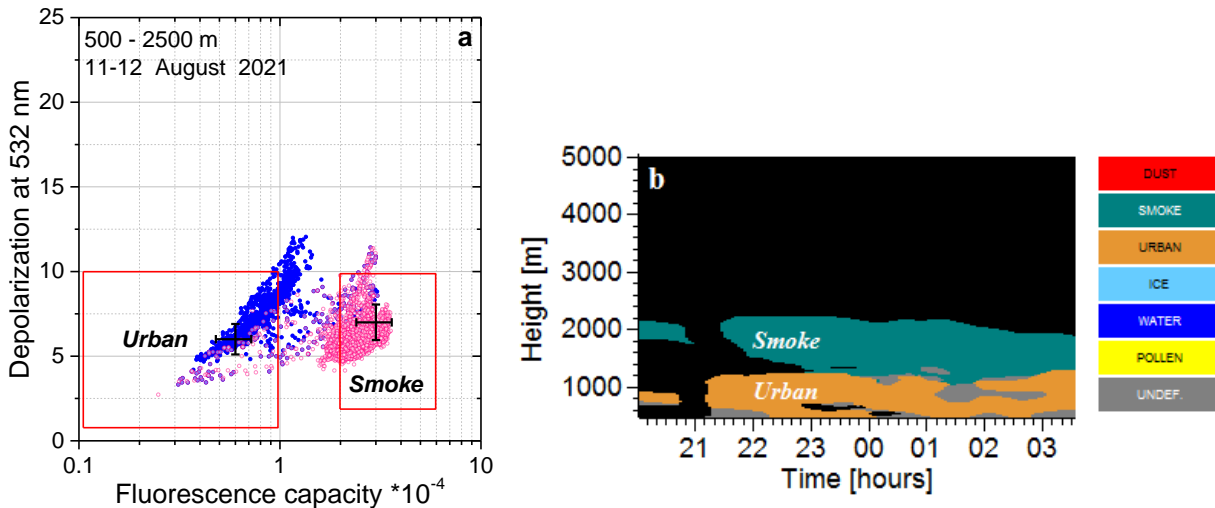


875

876

877 Fig.14. Spatio-temporal distributions of the backscattering coefficient β_{532} , the fluorescence
 878 backscattering coefficient β_F (in $10^{-4} \text{ Mm}^{-1}\text{sr}^{-1}$), the particle depolarization ratio δ_{532} , and the
 879 fluorescence capacity G_F in the night 11 – 12 August 2021. Measurements with $\beta_{532} < 0.2 \text{ Mm}^{-1}\text{sr}^{-1}$
 880 are marked by black color.
 881

882



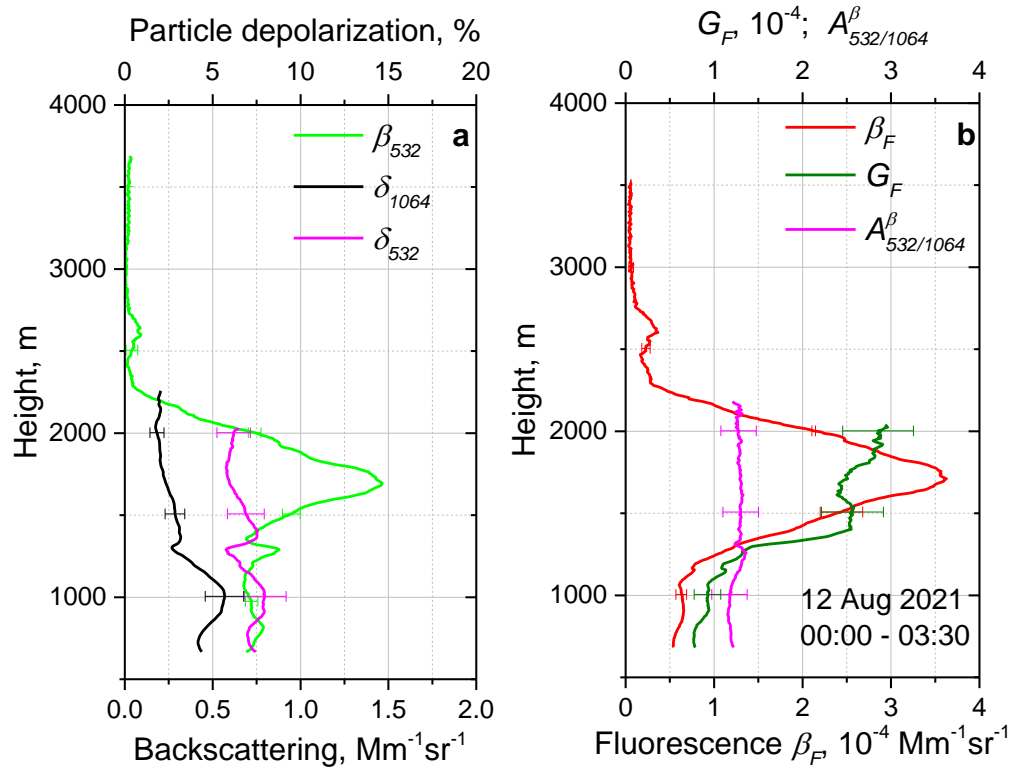
883

884 Fig.15. (a) The δ_{532} - G_F diagram for observations in 500 – 1400 m (blue symbols) and 1400 –
 885 2500 m (pink symbols) height ranges. (b) Spatio-temporal distribution of aerosol types in the
 886 night 11-12 August 2021.
 887

886

887

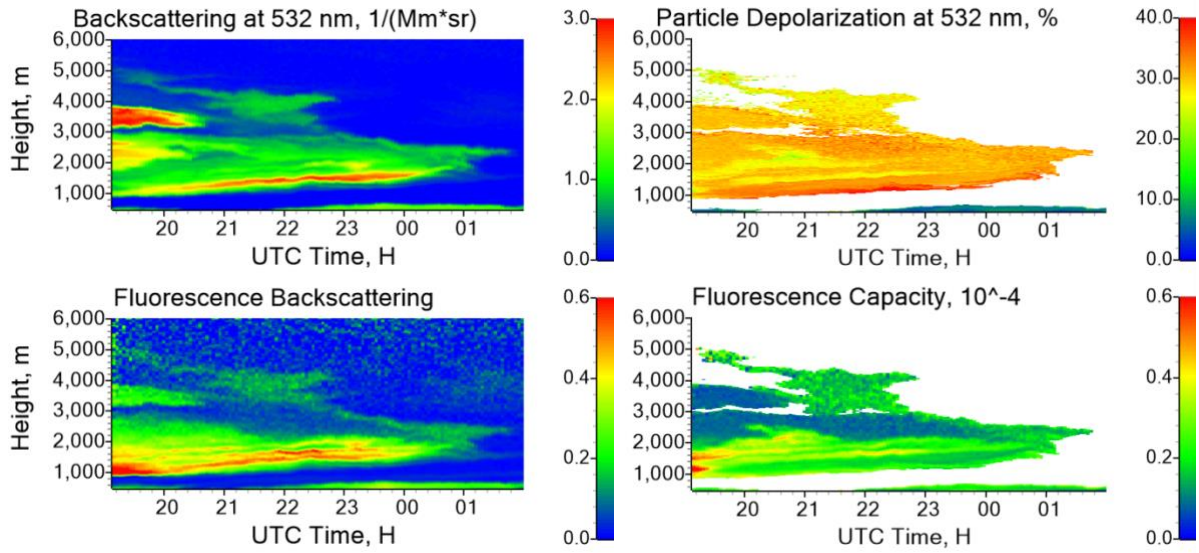
888
889



890
891
892
893
894
895

Fig.16. Vertical profiles of (a) backscattering coefficient β_{532} and particle depolarization ratios δ_{532} , δ_{1064} ; (b) fluorescence backscattering β_F , fluorescence capacity G_F and backscattering Angstrom exponent $A_{532/1064}^\beta$ on 12 August 2021 for period 00:00 – 03:30 UTC.

896



897

898

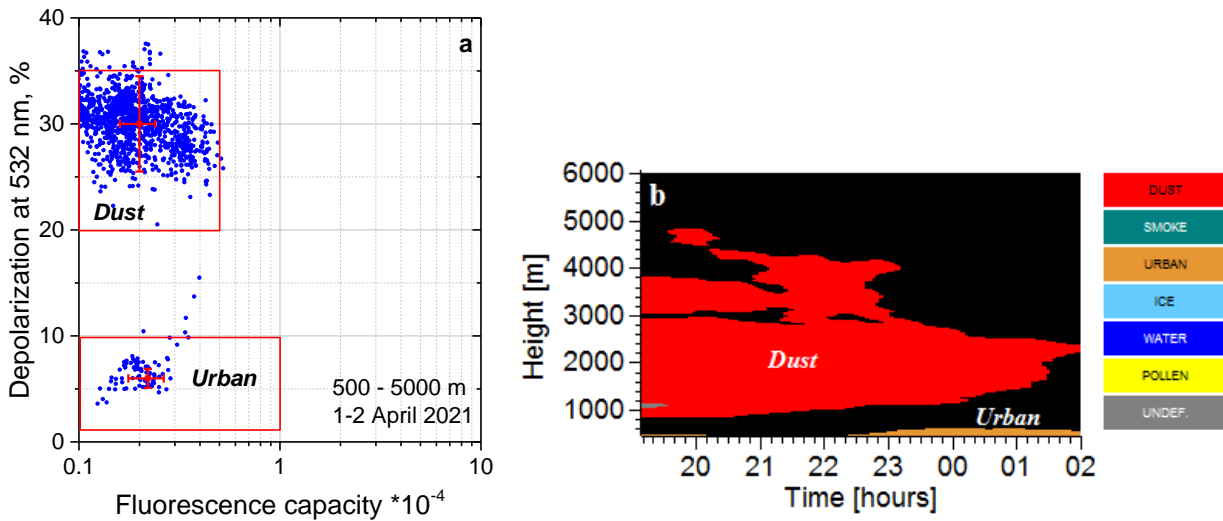
899

900

901

902

Fig.17. Height – temporal distributions of the backscattering coefficient at 532 nm β_{532} , the fluorescence backscattering coefficient β_F (in $10^{-4} \text{ Mm}^{-1}\text{sr}^{-1}$), the particle depolarization ratio at 532 nm δ_{532} , and the fluorescence capacity G_F in the night 1-2 April 2021.



903

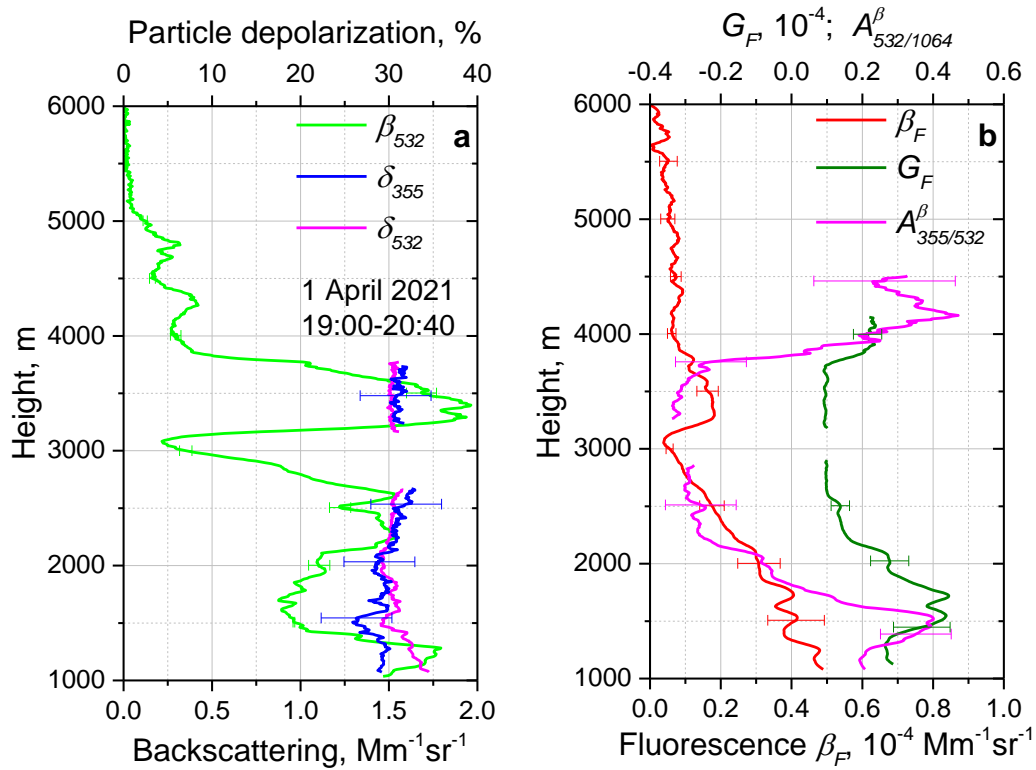
904

905

906

907

Fig.18. (a) The δ_{532} - G_F diagram for observations in 500 – 5000 m height range and (b) spatio-temporal distribution of aerosol types in the night 1-2 April 2021.



909

910

911

912

913

914

915

Fig.19. Vertical profiles of (a) backscattering coefficient β_{532} and particle depolarization ratios δ_{532} , δ_{355} ; (b) fluorescence backscattering β_F , fluorescence capacity G_F and backscattering Angstrom exponent $A_{355/532}^\beta$ on 1 April 2021 for period 19:00 – 20:40 UTC.

916 Table 1. Ranges of particle depolarization δ_{532} and fluorescence capacity G_F , which were used for aerosol classification.

Aerosol type	δ_{532} , %	G_F , ($\times 10^{-4}$)
Dust	20 - 35	0.1 – 0.5
Pollen	15 - 35	0.8 – 3.0
Urban	1 - 10	0.1 – 1.0
Smoke	2- 10	2.0 – 6.0
Ice	>40	<0.01
Water	<5	<0.01

917

918

919

920 Table 2. Intensive particle parameters such as the lidar ratios (S_{355} , S_{532}), particle depolarization ratios (δ_{355} , δ_{532} , δ_{1064}), extinction
 921 ($A_{355/532}^\alpha$) and backscattering ($A_{355/532}^\beta$, $A_{532/1064}^\beta$) Angstrom exponents for six episodes, analyzed in this work. Parameters are given for
 922 chosen height – temporal intervals and the types of aerosol are determined from fluorescence measurements.

Date	Time, UTC	H, km	Type	S_{355} , sr	S_{532} , sr	δ_{355} , %	δ_{532} , %	δ_{1064} , %	$A_{355/532}^\alpha$	$A_{355/532}^\beta$	$A_{532/1064}^\beta$
10.04.2020	21:00-23:00	0.9-1.1	Urb.+Poll.	48±7	48±7	5.0±1.0	6.0±1.0	10±1.5	1.3±0.2	1.4±0.2	1.0±0.2
		2.0-2.2	Urban	50±7	70±10	7.0±1.0	3.5±0.7	3.0±0.6	1.1±0.2	2.0±0.2	1.2±0.2
30.05.2020	21:00-02:00	1.8-2.0	Urban	60±9	55±8	3.6±0.8	4.0±0.8	5.7±1.0	2.0±0.2	1.6±0.2	1.2±0.2
12.09.2020	20:00-23:00	3.2-3.8	Smoke	50±7	80±12	4.5±1.0	3.0±0.6	2.0±0.4	1.0±0.2	2.2±0.2	1.2±0.2
15.09.2020	00:00-04:00	1.4-1.6	Pollen	40±6	37±6	9.5±1.5	8.0±1.5	15±2.5	1.6±0.2	1.4±0.2	0.9±0.2
		5.8-6.2	Smoke	45±7	70±10	9.0±1.5	3.5±0.7	1.4±0.3	0.8±0.2	2.0±0.2	1.2±0.2
01.04.2021	19:00-20:40	2.25-2.5	Dust	57±8	52±8	30±4.5	30±4.5	-	0±0.2	-0.3±0.2	-
11.08.2021	22:00-24:00	1.0-1.2	Urban	42±7	55±8	-	8.0±1.2	5.7±0.8	1.3±0.2	1.5±0.2	1.1±0.2
		1.5-2.0	Smoke	45±7	72±11	-	6.0±0.9	2.5±0.5	1.0±0.2	2.2±0.2	1.2±0.2

923

924

925
926
927
928

Table 3. Intensive particle parameters from publications of Burton et al., (2013); Nicolae et al., (2018); and Papagiannopoulos et al., (2018) together with values observed in current study for the urban, smoke and dust particles.

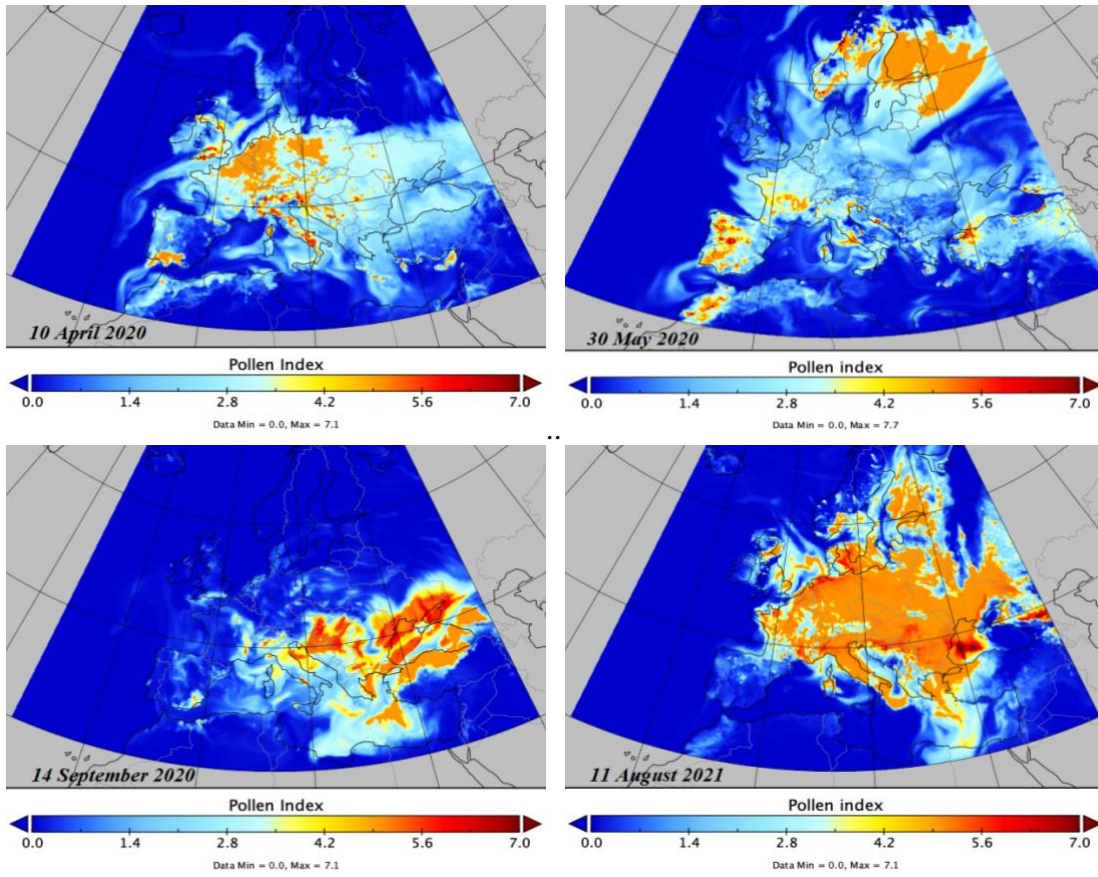
	Burton et al., 2013	Nicolae et al., 2018	Papagiannopoulos et al., 2018	This study
	Urban	Continental (rural)	Clear continental	Urban
S_{355} , sr		43-54	50±8	42 - 60
S_{532} , sr	43-81	52-53	41±6	55 -70
$A_{355/532}^{\alpha}$	-	1.2-1.3	1.7±0.6	1.1 -2.0
$A_{355/532}^{\beta}$	-	1.0-1.6	1.3±0.3	1.5 - 2.0
$A_{532/1064}^{\beta}$	0.49-1.3	0.54 – 1.0	1.0±0.3	1.1 - 1.2
Smoke				
S_{355} , sr	-	56-72	81±16	40 - 50
S_{532} , sr	46-87	81-92	78±11	70 - 80
$A_{355/532}^{\alpha}$	-	1.1-1.3	1.3±0.3	0.8 - 1.0
$A_{355/532}^{\beta}$	-	1.4 -2.1	1.2±0.3	2.0 - 2.4
$A_{532/1064}^{\beta}$	0.48-1.6	0.7-0.8	1.3±0.1	1.2
Dust				
S_{355} , sr	-	43-46	58±12	57
S_{532} , sr	41-57	44-49	55±7	52
$A_{355/532}^{\alpha}$	-	0.88-0.92	0.3±0.4	0
$A_{355/532}^{\beta}$	-	0.91-0.97	0.3±0.2	-0.3
$A_{532/1064}^{\beta}$	0.49-0.68	0.16-0.22	0.4±0.1	-

929
930

931 **Appendix.** Pollen index provided by SILAM

932
933 The SILAM is a chemical transport model, developed by the [Finnish Meteorological](#)
934 [Institute](#) (Sofiev et al., 2015). It provides information on atmospheric composition, air quality, and
935 pollen. In the pollen module of SILAM, six pollen types (alder, birch, grass, mugwort, olive,
936 ragweed) are considered. The pollen index is defined as a quantitative measure of the severity of
937 the pollen season and a proxy of the allergenic exposure (Sofiev et al., 2012, 2017). This higher
938 the pollen index is, the more pollen grains in the atmosphere and the higher allergy risk. Fig. A1
939 shows the maps of pollen index in 4 cases. According to the description of SILAM model, the
940 pollen index is labeled as “very high”, when its value is greater than 4.0.

941



942

943

944

945 Fig.A1. Pollen index provided by SILAM for 10 April 2020, 30 May 2020, 14 September 2020
946 and 11 August 2021. The levels of pollen index are – very low (<1.0), low (<2.0), moderate (<3.0),
947 high (< 4.0) and very high (>=4.0).

948

949

950